2022-03

Persulfate-based advanced oxidation processes: The new hope brought by nanocatalyst immobilization

Guo, R

10.1016/j.efmat.2022.05.004
Environmental Functional Materials
Elsevier BV

Persulfate-based advanced oxidation processes: The new hope brought by nanocatalyst immobilization

Ruonan Guo[1,2], Beidou Xi[1,2], Changsheng Guo[1], Xiuwen Cheng[3], Ningqing Lv[1], Wen Liu[4], Alistair G. L. Borthwick[5,6], Jian Xu[1,*]

1 *State Key Laboratory of Environmental Criteria and Risk Assessment, Chinese Research Academy of Environmental Sciences, Beijing 100012, P. R. China*

2 *School of Environment, Tsinghua University, Beijing 100084, P. R. China*

3 *Key Laboratory for Environmental Pollution Prediction and Control, Gansu Province, College of Earth and Environmental Sciences, Lanzhou University, Lanzhou 730000, P. R. China*

4 *College of Environmental Sciences and Engineering, The Key Laboratory of Water and Sediment Sciences (Ministry of Education), Peking University, Beijing 100871, P. R. China*

5 *Institute for Infrastructure and Environment, School of Engineering, The University of Edinburgh, Edinburgh EH9 3FG, UK*

6 School of Engineering, Computing and Mathematics, University of Plymouth, Plymouth PL4 8AA, UK

Corresponding author: Jian Xu
E-mail: xujian@craes.org.cn

Abstract:

Persulfate-based advanced oxidation processes (persulfate-AOPs) offer great promise for environmental remediation, with heterogeneous catalysts providing the backbone of many wastewater purification technologies. Unlike conventional nanocatalyst heterogeneous systems, the immobilized-catalyst system can bypass the separation problem to reduce scour and prevent aggregation by anchoring nanoparticles onto porous or large-particle carriers. This review presents the state-of-the-art of knowledge concerning immobilization methodologies and reactors, reaction mechanisms, and activation performance. Immobilization techniques onto supports are summarized and discussed, including membrane-based reaction systems (immersion mode, and filtration mode), electrocatalytic auxiliary systems, and alternative supports (metallic glasses, aerogels, hydrogels, and specific materials). Key scientific problems and important prospects for the further development of immobilized catalysts are outlined.

Keywords: advanced oxidation process; nanocatalyst immobilization; persulfate; wastewater treatment

Table Summary of abbreviations

Full Text	Abbreviation
Persulfate-based advanced oxidation processes	persulfate-AOPs
Advanced oxidation processes	AOPs
Reactive oxygen species	ROS
Peroxymonosulfate	PMS
Peroxydisulfate	PDS
Reduced graphene oxide	rGO
Polyvinylidene fluoride	PVDF
Polyacrylonitrile	PAN
Scanning electron microscope	SEM
S, N-doped carbon and iron nanoparticles	NSC-Fe
Layered double hydroxides	LDH
Nanofibers	NFs
Metal-organic frameworks	MOFs
Cellulose nanofibers	CNFs
Electrospun nanofibers	ENFs
Zero-valent iron	ZVI
Metallic Cu-doped C/SiO_2 nanofibers	CINMs
Ag-$La_{0.8}Ca_{0.2}Fe_{0.94}O_{3-\delta}$	Ag-LCF
Zeolitic imidazolate framework	ZIF
Calotropis gigantea fiber	CGF
Carbon nanotubes	CNTs
N-doped microtubule composites/PVDF	CFP
Biomimetic polydopamine	PDA
Polypropylene	PP
Total dissolved solids	TDS
Poly tetrafluoroethylene	PTFE
Metallic glass(es)	MGs/MG
Ultraviolet-visible light	UV-Vis
Three-dimensional	3D
Co-doped carbon aerogels	CoCA
Selective laser melting	SLM
Isotropic $CoFe_2O_4$@graphene hybrid aerogel	CFO@GA-I
Anisotropic $CoFe_2O_4$@graphene hybrid aerogel	CFO@GA-A
Graphene hybrid aerogel	GA
Polyacrylic acid	PAA
Graphene oxide	GO
Chemically bonded Co_3O_4 nanoflowers sponge	SP-50
Double-network hydrogel templated FeS/graphene	DMG
Polyvinyl alcohol	PVA

TiO_2 nanotubes	TNTs
$CoFe_2O_4$ on quartz sand support	$CoFe_2O_4$-QS
In situ chemical oxidation	ISCO
Capacitive deionization	CDI
Multiwalled carbon nanotube	MWCNT
Activated carbon fiber	ACF
Electro PDS	E-PDS
Electro PMS	E-PMS
Carbon fiber paper	CFP
Carbon fiber	CF
Flow-through cathode	FTC
Flow-by cathode	FBC
Asymmetric quasi capacitive deionization	AQCDI
Covalent organic frameworks	COFs
Natural organic matter	NOM
Polyethersulfone	PESF
1-methyl-2-pyrrolidinone	NMP
CoFe alloy and $CoFe_2O_4$ encapsulated in N-doped microtubes	CoFe-NMTs
Carbon black nano-spheres	CBNS

1. Introduction

The importance of water safety for economic development and public and environmental health cannot be overstated. Yet, despite rising levels of contamination and salinity of inland freshwater [1], more than 650 million people currently lack access to safe water [2]. Common natural pollutants, including pathogenic microorganisms, earth-derived heavy metals, cyanobacterial toxins, and metal-like substances (e.g., arsenic), can be removed through traditional water treatment methods (i.e., filtration and precipitation) [2]. However, the application of these basic technologies is limited by throughput requirements. Furthermore, priority pollutants and emergent contaminants have been found in natural streams, drinking water sources, and even sewage treatment plant effluents, thus posing a threat to human and ecosystem health. This is exacerbated by the proliferation and discharge of multidrug-resistant bacteria in certain sewage treatment plants, leading to health risks and reduced productivity [3-5]. The foregoing highlight the need for technological innovation and resilience to improve inefficient water treatment infrastructure.

Advanced oxidation processes (AOPs) provide a powerful means of degrading and even mineralizing refractory organic pollutants through the induction of reactive oxygen species (ROS), thus avoiding the need for further treatment of contaminant-laden sorbents or membrane concentrate streams [6]. In general, hydroxyl radicals (•OH) [7, 8], sulfate radicals ($SO_4^{\bullet-}$) [9, 10], chlorine radicals (Cl• and $Cl_2^{\bullet-}$) [11, 12], and radicals that enable direct electron transfer possess [13] can achieve rapid

decomposition of various organic pollutants and pathogenic bacteria. Owing to their lack of pH dependency and selective oxidation, persulfate-based advanced oxidation processes (persulfate-AOPs) have begun to receive more research attention than standard Fenton systems. Nanomaterials have provided an immense impetus as heterogeneous catalysts for peroxymonosulfate (PMS, $2KHSO_5 \cdot KHSO_4 \cdot K_2SO_4$) and peroxydisulfate (PDS, $Na_2S_2O_8$ or $K_2S_2O_8$) activation. The key mechanism behind the persulfate heterogeneous activation reaction is the direct transfer of electrons from catalysts to persulfate ions (labeled as "Radical mechanism" in **Fig. 1**). Researchers have recently proven the existence of a non-radical oxide pathway (marked as "Non-radical mechanism" in **Fig. 1**), involving a direct electron transfer process, reaction with surface-activated complex (or surface-confined radical), direct oxidation of high-valence metals, and the participation of singlet oxygen in the catalytic oxidation of organic contaminants [14-16].

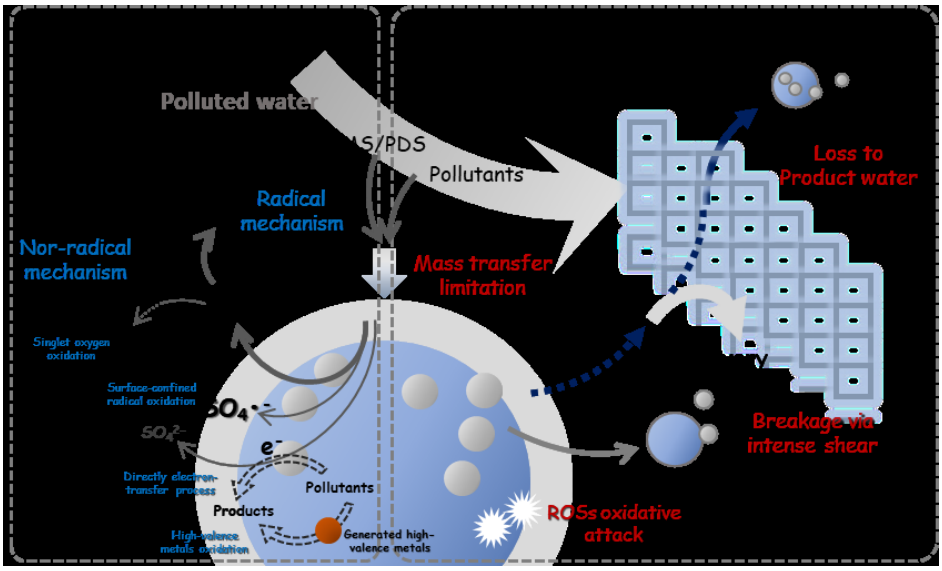

Fig. 1. Heterogeneous activation mechanism of persulfates, and challenges to nanocatalysts in persulfate-based-AOPs.

However, nanocatalyst loss to product water, mass transfer limitations, ROS

oxidative attack, and breakage under intense shear are almost inevitable in a nanoparticle catalytic system [17, 18]. Although nanotechnology cannot solve all water treatment problems, nanomaterials might enable the development of next-generation engineered water purification systems, which are compact and simple to deploy [2, 19]. Immobilization has recently been reported to help minimize leaching, inducing an obvious degradation effect and reducing the cost associated with separation of nanocatalysts, thus leading to more effective application of nanoparticle-based AOPs for water remediation [20-22]. The future development of persulfate-AOPs depends on the optimization and immobilization of nanocatalysts in addition to reactor design. For instance, reduced graphene oxide doped with nitrogen/polyvinylidene fluoride matrix (rGO-N-PVDF) composite membrane was prepared and used in a specific filtration system with compact structure, convenient operation, and easy recovery in water treatment [23]. Conversion of pharmaceuticals in the range 54%–91% was then obtained even after 24 h of operation in full continuous mode, thus demonstrating the activation performance of rGO-N-PVDF for PDS conversion. However, the pollutant removal efficiency decreased in preliminary experiments using surface water compared to those using ultrapure water. Therefore, this research field presents both opportunities and challenges, requiring more comprehensive scientific research in the future.

Simultaneous specific reaction systems and reactors have recently been established, mainly based on a surface reaction system formed from composite material and a synergistic filtration system, as shown in **Fig. 2**. These can be directly supplemented with light and heat sources to achieve more efficient, faster wastewater

treatment [16, 24, 25]. Nevertheless, specially designed reactors are required in electrocatalytic auxiliary systems (examples shown in **Fig. 2**). This review describes the current state of knowledge of persulfate activation methods, different immobilization methodologies and reactors, reaction mechanisms, and activation performance. Challenges and future prospects are discussed, including the lack of a universal optimization principle for catalyst preparation and reactor design, and the use of blank standardized experimental methods in various complex water matrices which ignore cost and life-cycle effects. The overall goal is to gain insight into design approaches for next-generation multifunctional treatment systems that reduce water pollution and energy consumption.

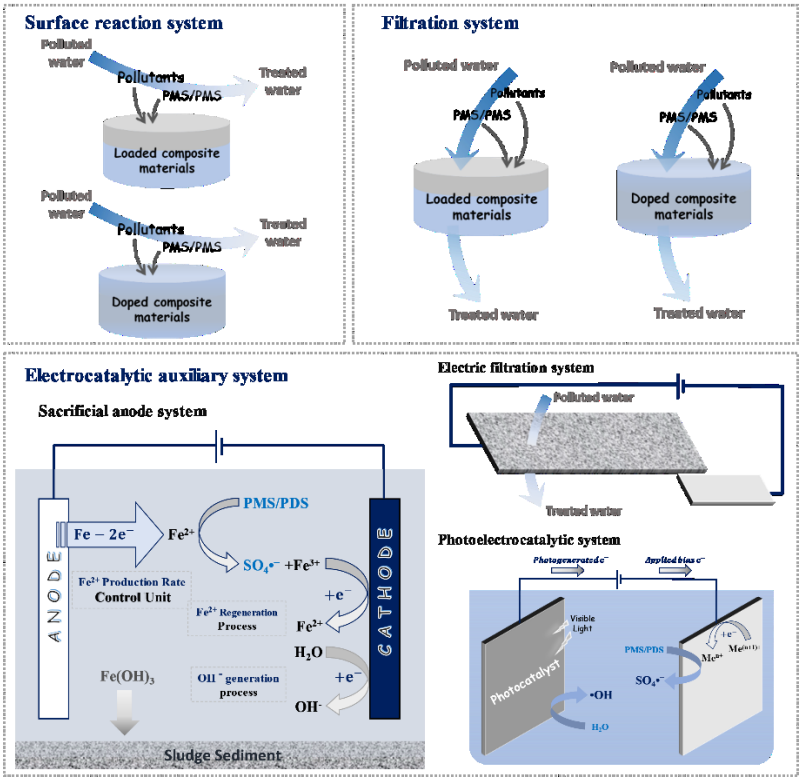

Fig. 2. Construction strategy for persulfate activation systems based on immobilized nanocatalysts.

2. Membrane-based reaction systems

2.1 Immersion mode reaction systems

The working pH in a PMS activation system is harsh; thus, the standards for catalyst stability and raw membrane material are higher compared to other systems. Moreover, maintenance of catalytic performance relies on the redox reaction (i.e., metal valence state transformation), whereas very strong nanoparticle-support interactions between the support and nanoparticles usually make it difficult to reduce nanoparticles. Based on their superior characteristics in terms of long life-span, thermal stability, and excellent tolerance to pH, ceramic membranes have attracted much attention in recent years, as summarized in **Table 1**. For example, the composite membrane covered with polyacrylonitrile (PAN)-Co-C and a Co/C layer shown in **Figs. 3(a-1)–(a-4)** has a porous surface and cross-section [26]. The catalysis performance of such membranes has been ascribed to abundant active functional sites (C, N, and Co), thus importing an intrinsic antifouling effect in the membrane filtration process. The formation of a chemical bond between the C/Co layer and Al_2O_3 results in more robust functionalized membranes with stable catalytic performance. However, these ceramic membranes are extremely brittle, which means that they can easily break and disperse during application. Moreover, the fragments are difficult either to collect or to recover.

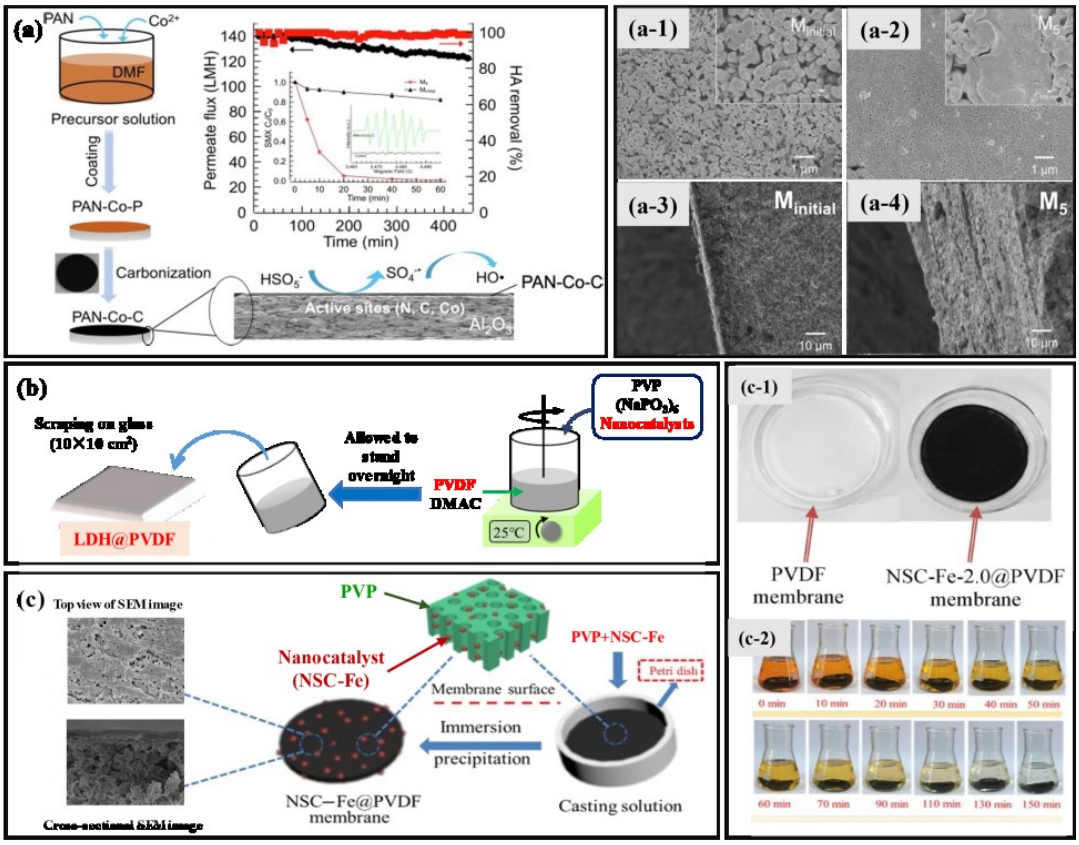

Fig. 3. Typical composite membrane prepared via ceramic and polymeric substances, and then used in immersion mode reaction systems: (a) synthetic procedure for PAN-Co ceramic membrane, with SEM surface images of (a-1) initial Al_2O_3 membrane, and (a-2) functionalized PAN-Co-C membrane, and SEM cross-section images of (a-3) initial Al_2O_3 membrane, and (a-4) functionalized PAN-Co-C membrane (reprinted with permission from [26], copyright 2019 Elsevier); (b) synthetic procedure for LDH@PVDF membrane (reprinted with permission from [27], copyright 2020 Elsevier); and (c) synthetic procedure for NSC-Fe@PVDF membranes, with (c-1) digital photograph of NSC-Fe@PVDF membrane and (c-2) color changes of Orange II in NSC-Fe@PVDF/PMS system (reprinted with permission from [28], copyright 2017 Elsevier).

Generally, polymeric substances are easy to synthesize and manufacture; thus, they play an important part in nanocatalyst immobilization. In particular, composite membranes fabricated via polymeric substances show great suppleness, which means that they can be collected and washed using a simple treatment process (see **Table 1**) to achieve recycling of catalytic materials. Polyvinylidene fluoride (PVDF) is a

promising membrane substrate that features: (i) great physical and chemical stability, allowing it to be applied under a wide range of conditions; (ii) excellent flexibility, enabling it to be processed into different shapes; and (iii) cost-effectiveness and eco-friendliness. As shown in **Figs. 3(b) and (c)**, hybrid catalytic PVDF membranes are readily fabricated by the phase inversion technique. For instance, the functionalized, pure, white PVDF membrane appears black after being doped by iron nanoparticles embedded in S, N-cooped carbon (**Fig. 3(c-1)**), demonstrating a uniform distribution of nanocatalysts [28]. The synergistic effect between S, N-doped carbon, and iron nanoparticles (NSC-Fe) improves the catalytic ability of NSC-Fe@PVDF; thus, substantial decolorization of orange II occurs with low metal leaching (**Fig. 3(c-2)**). **Table 1** lists data that confirm the great activation performance and durability of layered double hydroxides (LDH)@PVDF and the CuO@CuS/PVDF membrane.

During the heterogeneous catalytic reaction, the degradation effect of target pollutants correlates positively with the interaction between PMS and catalyst. Therefore, catalyst with high specific surface area and porosity is required, in order to promote interaction with PMS [29]. Nanofibers (NFs) are widely considered to be a promising support for nanoparticle immobilization because of their high surface area. Generally, nanocatalysts immobilize uniformly and tightly on the surface of NFs when exposed to reactants, such as oxidizing agents, contaminants, and coexisting ions or organic matter [27, 30]. With their large continuous surface area and high flexibility, NFs can form random arrays and macroscopic mats, which are beneficial for catalyst separation, recovery, and reuse [31]. **Fig. 4(a)** illustrates vacuum filtration, an efficient

method for loading Co/Fe metal−organic framework (MOF) nanocatalysts onto cellulose nanofiber (CNF) membranes [32]. Due to the two redox cycles of Co (II-III-II) and Fe (II-III-II) in Co/Fe MOFs nanoparticles, $SO_4^{\bullet-}$ is continually induced through PMS activation to degrade pollutants. CNFs simultaneously solve the problem of nanocatalyst agglomeration (**Fig. 4(b)**) and functionalized membranes can be easily collected from the solution. As shown in **Fig. 4(c)**, CNFs have also been used as a template to prepare magnetic nanocatalysts with uniform size distribution via filtration [33]. Given their high concentration of magnetic Fe_3O_4 nanoparticles, the flexible magnetic membranes exhibited superparamagnetic properties and persulfate of high activation performance, thereby facilitating convenient recovery of the composite membrane (in **Table 1**) avoiding loss of nanoparticles. Even so, further information is required on the mineralization efficiency of pollutants, metal leaching concentration, and catalytic stability.

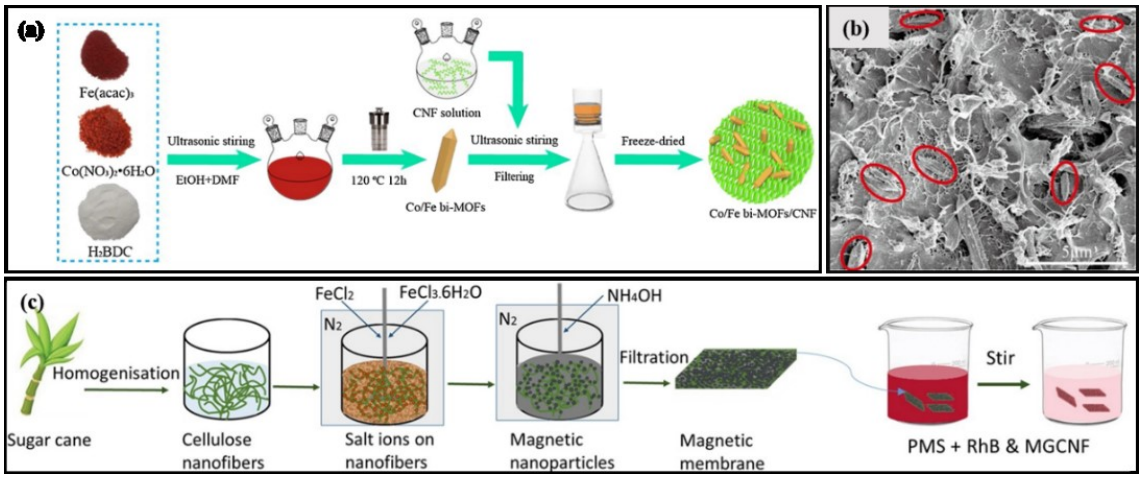

Fig. 4. Typical composite membrane prepared from nanofibers through filtration, and used in immersion mode reaction systems: (a) synthetic procedure, (b) SEM image of Co/Fe bi- MOFs/CNFs membrane (reprinted with permission from [32], copyright 2020 Elsevier); and (c) schematic representation of magnetic nanocellulose membrane preparation and PMS activation process (reprinted with permission

from [33], copyright 2020 Elsevier).

Thus far, owing to the absolute discontinuity of nanoparticles, the mechanical properties of the foregoing composite membrane prepared by vacuum filtration are much lower than those of existing advanced fiber-reinforced composites [34, 35]. Electrospinning is a technique that produces continuous NFs by jetting polymer solutions in high electric fields, thus providing excellent control over NF dimensions and orientation, as illustrated in **Fig. 5(a)** [36]. Compared with nanofibers synthesized using other methods, electrospun nanofibers (ENFs) provide overwhelming benefits, including: (i) potential for controllable synthesis; (ii) large specific surface area, high aspect ratio, and oriented charge transfer pathways; (iii) excellent compositional and structural stability; and (iv) cost control of mass production, especially for multicomponent composite fibers, suitable for industrial application [37]. A previous study synthesized composite α-Fe@carbon ENFs by co-electrospinning and pyrolysis self-reduction [38]. In **Fig. 5(a)**, small particles of average diameter … nm could be observed on the surface of the fiber, demonstrating that iron species were distributed uniformly and welded firmly in the fibrous scaffolds. Based on active zero-valent iron (ZVI), the ENFs exhibited excellent PMS activation activity, high stability, and easy magnetic separation during the contaminant removal process. However, the flexible ENF membranes (nonporous or microporous, < 2 nm) were unable to provide sufficient active sites for pollutant adsorption and ROS transportation, thus limiting further improvement in catalytic capability [39, 40].

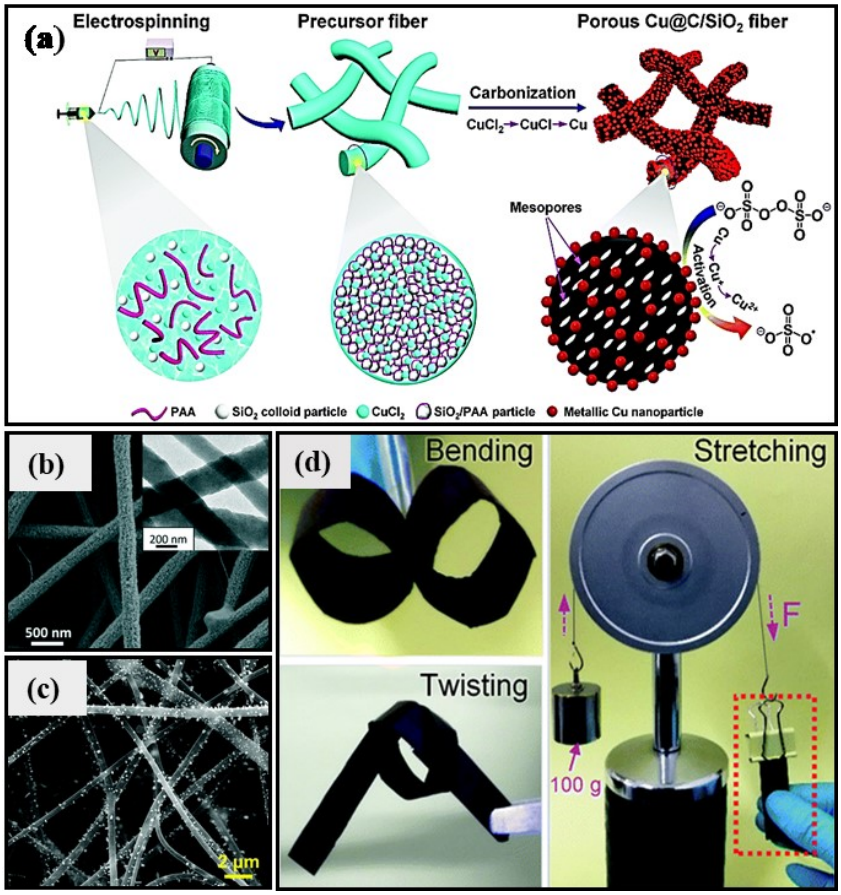

Fig. 5. Typical composite membrane prepared from electrospun nanofibers, and used in immersion mode reaction systems: (a) synthetic procedure for metallic Cu-doped C/SiO_2 nanofibers (CINMs) by sol-gel electrospinning method; (b) SEM image of α-Fe@carbon ENFs (reprinted with permission from [38], Copyright 2017 RSC); (c) SEM image of CINMs; and (d) optical photograph showing that the CINMs could be folded into a paper crane without any fracturing (reprinted with permission from [39], copyright 2019 RSC).

A recent study of inorganic membranous catalysts that have extraordinary flexibility and large mesopores by Shan et al. [39] has provided convincing evidence for the improvement of their catalytic oxidation activity in persulfate-AOPs. Shan et al. successfully fabricated Cu@C/SiO_2 nanofiber membranes (CINMs) through electrospinning and *in situ* carbonization (**Figs. 5(c)** and **(d)**). As indicated in **Fig. 5(c)**, the synthesized nanoparticles were able to break through the ground and become firmly fixed on the NFs surface, indicating the structural stability of the resultant membranes

198 and the validity of the electrospinning method. Furthermore, the as-obtained CINMs,
199 which have large mesopores and are very flexible, can withstand large bending and
200 torsional deformations with no detectable fractures (see **Fig. 5(d)**). This synthetic
201 strategy therefore overcomes the obstacles of brittleness and the poor mechanical
202 properties of crystalline inorganic NF membranes, and can be further extended to other
203 metal-embedded inorganic membranes.

204 The integrated effect of randomly arranged NFs, sufficient hydroxyl groups, and
205 rough surfaces of nanostructures endows synthesized CINMs with superhydrophilicity,
206 a property conducive to water purification. Furthermore, as indicated in **Table 1**, novel
207 Co–Al_2O_3 and Pt–Al_2O_3 NFs membranes prepared using electrospinning have
208 demonstrated great flexibility and excellent PMS activation capability [41, 42]. Given
209 its flexible membrane form, the shape of Pt/Al_2O_3 can be adjusted for use in different
210 membrane reactors [42]. As for the reaction mechanism, PMS can be easily adsorbed
211 on the surface of Pt/Al_2O_3 fiber through its oxygen atom, due to the positive charge of
212 Pt/Al_2O_3 during the reaction process. Meanwhile, electron-rich organic molecules with
213 aromatic rings in the structure may also be adsorbed on the fiber and contribute
214 electrons to PMS through Pt as a medium, thereby leading to further destruction of
215 organic pollutants and gradual decomposition of PMS.

216 Ma et al. [43] processed Ag-$La_{0.8}Ca_{0.2}Fe_{0.94}O_{3-\delta}$ (Ag-LCF) into hollow fiber
217 membranes by means of a phase-inversion and sintering method. They examined the
218 reaction of the Ag-LCF hollow fiber membrane, whereby a methylene blue and
219 persulfate solution was pumped into the fiber lumen at a prescribed flow rate. SEM

images revealed pinhole defects and exposed particles that appeared on the inner surface with increasing grain size (see inset). The membrane wall, especially the dense membrane core, was kept intact to prevent wastewater from leaking from the cavity into the shell side. However, further measurements are still needed, including the mineralization efficiency of pollutants, metal leaching concentration, reusability, and active sites of Ag-LCF.

From the above collection of mixed systems based on catalytic membranes, a possible reaction mechanism has been identified, as depicted in **Fig. 6** [28, 32]. First, pollutant and persulfate ions (i.e., HSO_5^- and $S_2O_8^{2-}$) adsorb on active sites on the membrane surface. Next, surface adsorbed persulfate is activated by catalytic sites to induce ROS, and then interacts with adsorbed organic molecules and/or bacteria through an *in situ* reaction, after which the preoccupied sites are released. These released free sites accelerate the transfer of aqueous reactant, thereby initiating a new adsorption-oxidation cycle. The foregoing cycle repeats itself until most or all of the target pollutants are removed. The nano-size effect of metal particles and the relatively low diffusion resistance of organic matter on the surface of catalytic membranes are conducive to full contact between organic matter and active sites, which is beneficial to the catalytic performance of the membrane [28]. For carbon-based and carbon-doped catalytic membranes, the work function of metal nanoparticles embedded in carbon is lower than that of a carbon surface due to facile electron transfer from the metallic active sites to the carbon atom [44]. At the same time, the carbon shell forms a reservoir that effectively delays the process of iron dissolution (in the solution). Hence, such

composite membranes intrinsically display enhanced stability and excellent catalytic performance. However, organic molecules and persulfate ions experience difficulty in entering the catalytic membrane pores in batch mode (**Table 1**), which prevents full utilization of the possible active sites in the membrane pore walls (see **Fig. 2**). An alternative approach is to assemble the composite membranes in the filtration reactor, enabling the internal active sites to be properly exploited.

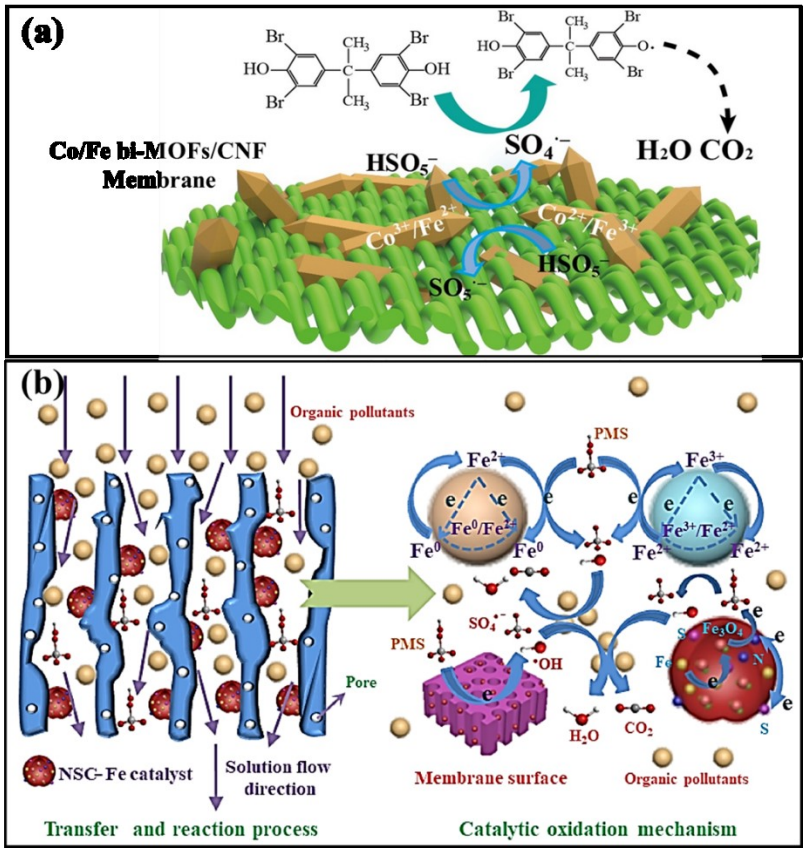

Fig. 6. Schematic illustration of reaction mechanism for organic removal by (a) Co/Fe bi-MOFs/cellulose NFs membrane/PMS system (reprinted with permission from [32], copyright 2020 Elsevier), and (b) NSC-Fe@PVDF/PMS system (reprinted with permission from [28], copyright 2017 Elsevier).

2.2 Filtration mode reaction systems

Persulfate-AOPs can be used in conjunction with membrane filtration as a pretreatment stage to degrade organic compounds in the membrane feed stream. This

serves as a mixed/one-pot process and a post-treatment stage to demineralize non-rejected micropollutants in the infiltration stream and reduce organics in the concentrated liquid stream. It has been demonstrated that this series of combined processes (i.e., the filtration system in **Fig. 2**) can efficiently remove pollutants [45]. These treatment methods represent the latest developments in the field (**Table 2**). The following section discusses several advanced studies on the coupling of membrane filtration and persulfate-AOPs.

Wang et al. [46] established an *in situ* growth technique to produce a zeolitic imidazolate framework (ZIF)-67/PAN filter, in which the loading ZIF-67 retained its morphology, structure, and catalytic capacity in comparison to pure ZIF-67 powder. It has been confirmed that Co^{2+} in ZIF-67 can activate PMS to generate ROS for pollutant degradation. Moreover, a piece of ZIF-67/PAN filter (3.5 cm^2) can be installed in the Swinnex syringe filter bracket enabling the syringe pump to drive contaminated solution through the filter, achieving water purification (**Fig. 7(a)**). Likewise, CuCo LDH@PAN and CuCo LDH@calotropis gigantea fiber (CGF) composite membranes have been synthesized through vacuum filtration (**Fig. 7(b)**) by our group to enhance the applicability of highly efficient nanocatalysts [27]. In **Fig. 7(b)** the pure CGF membrane sample is white, and the composite membrane has a generally brown color, indicating a uniform distribution of CuCo LDH on the CGF scaffold. The morphology of the membrane surface changed visibly after the CuCo LDH coating, also indicating successful fabrication of the composite membrane. Results of controlled experiments revealed that the remarkable catalytic performance of both LDH@CGF and

LDH@PAN can be attributed to the excellent PMS activation capability of CuCo LDH. Nevertheless, the metal iron leaching property and stability of composite membranes with different nanocatalysts and/or supports warrant further, in-depth investigation.

The activation ability of catalytic membranes in dead-end filtration mode has been tested through full recirculation of the filtrate. **Fig. 7(c)** presents the recirculation mode as configuration A, and the continuous (non-recycling) mode experiments as configuration B [23, 47]. In the recycling filtration mode, the filtrate entered the feed tank under vigorous stirring, and samples were taken each membrane filtration cycle. By adjusting the transmembrane pressure and residence time, the nanocomposite membranes were able to control the degree of reaction in a manner that was easy to operate. As a key characteristic of membrane filtration [48], water flux is intimately linked to surface and structural features of the filter layer, which impact treatment efficiency and energy consumption during operation. Sheng et al. [51] illustrated that the water flux of the composite membrane increases in accordance with enhancement of the C/O ratio of the GO/carbon nanotubes (CNTs) mats, with the ratio exhibiting a linear relationship with the reduction degree of rGO flakes (**Table 2)**. Furthermore, Fan et al. [49] reported a new integrated system for phenol removal by combining a coal-based carbon tube membrane with persulfate-AOPs.

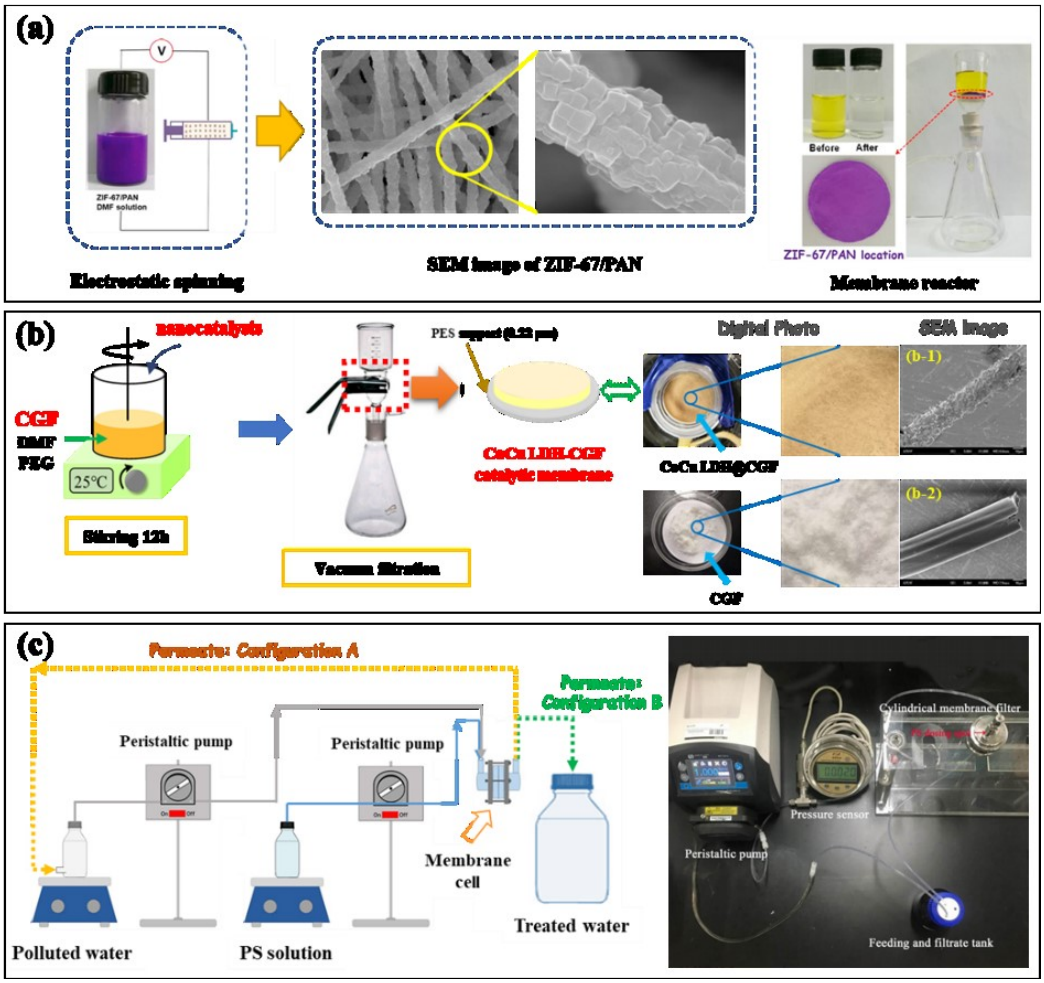

Fig. 7. Typical composite membranes used in filtration mode reaction systems based on vacuum filtration: (a) synthetic procedure, SEM images, and water treatment method for ZIF-67/PAN membrane (reprinted with permission from [50], copyright 2017 Elsevier); (b) synthetic procedure, SEM images, digital photos and water treatment method for CoCu LDH-CGF membrane and pristine CGF membrane. (reprinted with permission from [27], copyright 2020 Elsevier); and (c) schematic diagram of the experimental setup under recirculation mode (configuration A) and continuous mode (configuration B). (reprinted with permission from [23, 47], copyright 2019 and 2020 Elsevier); the digital photograph depicts elements in the filtration reaction system with recirculation and continuous modes (reprinted with permission from [51], copyright 2020 Elsevier).

However, composite membranes prepared by vacuum filtration have poor mechanical properties, which adversely impact on their long-term use in practice. As a possible solution, high-efficiency nanocatalysts with CoFe alloy and $CoFe_2O_4$

encapsulated in N-doped microtubule composites were fabricated and immobilized into PVDF (CFP) membrane [52]. The CFP membrane exhibited excellent superhydrophilicity and high flux (1 463.7 L/(m·h·bar), in accordance with SEM images (**Fig. 8(a)**). The foregoing indicate that the powder catalysts served as pore-forming agents to the PVDF membrane, thus allowing electrons to be transmitted quickly without being affected by high mass transfer resistance. As evident in **Table 2**, the CFP membrane achieves excellent, stable catalytic performance and low metal leaching. After adding PMS, the CFP membrane not only maintained a high removal rate of tetracycline degradation (more than 90%) in the humus coexistence system but also effectively eliminated the adverse effects of membrane pollution, thus demonstrating that the membrane possessed an excellent catalytic self-cleaning property. As illustrated in **Fig. 8(b)**, biomimetic polydopamine and ZIF-67 decorated polypropylene (PDA/ZIF-67@PP) membrane under Xenon lamp irradiation were filtered with feed solution consisting of contaminants and PMS at 1 bar pressure [53]. Abundant active sites, such as carboxyl, amide, and phenolic hydroxyl occur in the PDA layer, which can bind with Co ions during synthesis of ZIF-67. As a result, the membrane exhibited especially desirable properties of recyclability, antifouling, and self-cleaning during pollutant degradation. Hence, integration of catalytic oxidation technology with membrane technology offers a broad prospect for overcoming fouling [52, 53].

Another alternative water treatment unit design strategy is based on a fluidized bed. Zhu et al. [54] demonstrated that an optimized α-Fe_2O_3 nanodisk/bacterial

cellulose composite membrane attained excellent PMS photodegradation performance in both ordinary stirring and flowing bed states (**Fig. 8(c)**). Rich hydroxyl groups on the bacterial cellulose benefited the accommodation and dispersion of α-Fe_2O_3 nanodisks and helped enrich dyes on the surface. Furthermore, the membrane retained high catalytic efficiency, especially in the flowing bed condition, and achieved long-term durability over a range of flow rates. Compared to batch mode operation, the Fe_xO_y functionalized membrane/PDS system has been found to have higher degradation efficiency in the pressure filtration mode, as shown in **Fig. 8(d)** pathway A [55], and that the diffusion resistance of the reactants limited accessibility of Fe_xO_y located in the membrane matrix.

Apart from direct sewage treatment, functionalized membranes could be used more cost-effectively through combination with nanofiltration membrane-based separation to repair naphthenic acid in water containing highly concentrated total dissolved solids (TDS). As seen in **Fig. 8(d)**, a nanofiltration membrane can remove naphthenic acid from large volumes of produced water via pathway B, resulting in permeation comprised of discharge quality water (<10 mg/L) that leaves the operating unit via pathway A-1. Finally, the retentate stream should be treated by Fe_xO_y functionalized membrane/PDS system (AOP, pathway A-2) to meet the emission standards for naphthenic acid and discharge via pathway C.

Pollutants in the feed solution are limited near the catalyst surface when the feed passes through the active layer of the membrane by way of voids between the catalysts. In the surface reaction, the concentration of short-lived ROS is significantly higher than

that of the bulk. Thus, the pollutants are constantly and rapidly removed from the reaction zone, leading to a method of recovery of potable water that is more feasible, energy-intensive, and cost-effective. However, the amount of Fe leaching was very high (see **Table 2**). Therefore, further research, including long-term stability tests and technoeconomic analysis, is needed to verify the feasibility of the combination strategy in practical application.

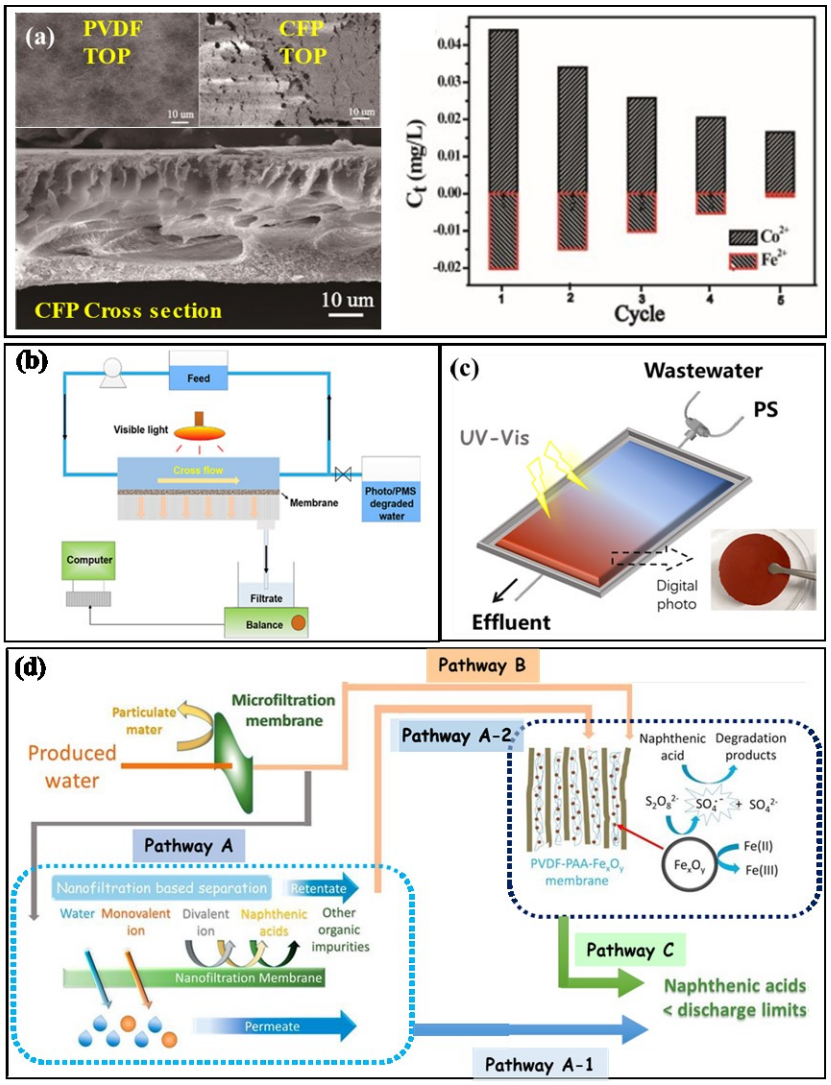

Fig. 8. Typical composite membrane used in filtration mode reaction systems based on cross-flow filtration: (a) top-section SEM images of pristine PVDF membrane and CoFe-NMTs-800/PVDF membrane, cross-section SEM image of CoFe-NMTs-800/PVDF membrane, and metal leaching concentration after five runs in CoFe-NMTs-800/PMS system (reprinted with permission from [52],

copyright 2021 Elsevier); (b) schematic representation of integration of nanofiltration membranes and Fe_xO_y functionalized membranes for treatment of naphthenic acid from produced water (reprinted with permission from [55], copyright 2017 Elsevier); (c) schematic depiction of the Flowing Bed Device (reprinted with permission from [54], copyright 2018 ACS); and (d) cross-flow filtration apparatus with light irradiation (reprinted with permission from [53], copyright 2019 Elsevier).

The carbon-based catalytic membrane is likely to become a substitute for metal catalysts, thus avoiding secondary pollution arising from metal leaching into the treated water. As discussed above, only three studies have employed carbon-based catalytic membranes in which the catalytically active phase is placed on top of a certain support (Polytetrafluoroethylene (PTFE) [47, 56] or nylon [51]). Vieira et al. [23] conducted a study of N-doped rGO (rGO-N) nanocatalysts, during which rGO-N-PTFE partially disintegrated during continuous operation and/or drying. By contrast, rGO-N-PVDFs exhibited structural and catalytic stability, demonstrating resistance toward fouling phenomena. However, the performance of the treatment process declined dramatically when surface water was used instead of ultrapure water in an early trial.

3. Specific materials systems

Metallic glasses (MGs) have grown in popularity in the field of wastewater remediation catalysis due to their great catalytic activity, high strength, elasticity, superior corrosion and wear resistance properties, and unique soft/hard magnetism [57, 58]. MG ribbons prepared by melt-spinning usually exhibit high efficiency, reusability, and sustainability [59]. Moreover, melt-spinning techniques have proved cost-effective when applied to industrial-scale water remediation [57].

Liang et al. [60] manufactured various iron-based MGs and applied them to persulfate activation systems. Unlike powder catalysts, MG ribbons present a metallic, flexible appearance (**Fig. 9(a)**) benefiting ease of operation, low cost, and control of excess reaction [60]. Moreover, as-obtained MGs in persulfate-AOPs have outstanding reusability, exceeding $Fe_{78}Si_9B_{13}$ MG [61, 62], $Fe_{73.5}Si_{13.5}B_9Cu_1Nb_3$ MG [63], and $Fe_{83}Si_2B_{11}P_3C_1$ MG by factors of 30, 10, and 35 (see **Fig. 9(b)**) [64]. Such a durable and efficient environmental catalyst has great potential in practical wastewater remediation. The exact mechanism by which atoms participate and electrons are transferred in MGs with amorphous structures is poorly understood, especially when MGs are used as a catalyst. Jia et al. [61] stated that persulfate activation can be attributed to ferrous (Fe^{2+}) in solution rather than in solid form in a $Fe_{78}Si_9B_{13}$/PDS/ultraviolet-visible light (UV-Vis) reaction system. Even so, in a more recent study [62], Liang et al. utilized ZVI as an electron donor to activate PDS and generate •OH and ferrous ions via a four-electron pathway involving water oxidation in $Fe_{78}Si_9B_{13}$ MG. Further reaction of Fe^{2+} with persulfate then produced $SO_4^{\bullet-}$. Similarly, in a $Fe_{78}Si_9B_{13}$/PMS/UV-Vis reaction system, direct surface corrosion of $Fe_{78}Si_9B_{13}$ ribbons by PMS generated $SO_4^{\bullet-}$. As the reaction progressed, ZVI on the $Fe_{78}Si_9B_{13}$ MG surface was consumed by persulfate to produce ROS (used for pollutant removal), after which UV-Vis irradiation accelerated the surface corrosive process. Buried Fe was gradually covered by SiO_2, which in turn gradually changed from Si on the ribbon surface during persulfate activation, thus preventing further iron leaching. During mechanical stirring, SiO_2 was easily shaken off, meaning that $Fe_{78}Si_9B_{13}$

ribbons could react with peroxide when necessary, thereby realizing the high reusability of $Fe_{78}Si_9B_{13}$ ribbons. However, when the service time was over 30 cycles, the $Fe_{78}Si_9B_{13}$ ribbon became gradually exhausted due to the lack of a SiO_2 layer to prevent further iron leaching, causing secondary pollution of the dye solution [61].

In recent years, three-dimensional (3D) printing, also known as additive manufacturing, has emerged as a novel method for simplifying the single process of material manufacture. Liang et al. [60] successfully prepared Fe-based MGs with 3D diamond dodecahedron microstructure using selective laser melting (SLM) according to a predesigned 3D computer-aided design model (**Fig. 9(c)**). Their results showed that efficiency remained almost unchanged after being used repeatedly 45 times, and that the surface after use was still as fresh as the original MG matrix composite. The ultra-stable reusability of the MG matrix composite in persulfate-AOPs means that it currently has the greatest reusability and catalytic potential among prospective catalysts. Moreover, it is likely that even higher reusability will be achieved in future.

Follow-up studies have focused on optimizing the catalytic performance of MGs by accurately regulating their chemical composition and atomic structure. Even so, the link between structural heterogeneity and catalytic performance of MGs still needs to be confirmed, and the mechanism (or origin) behind their high catalytic performance has yet to be identified.

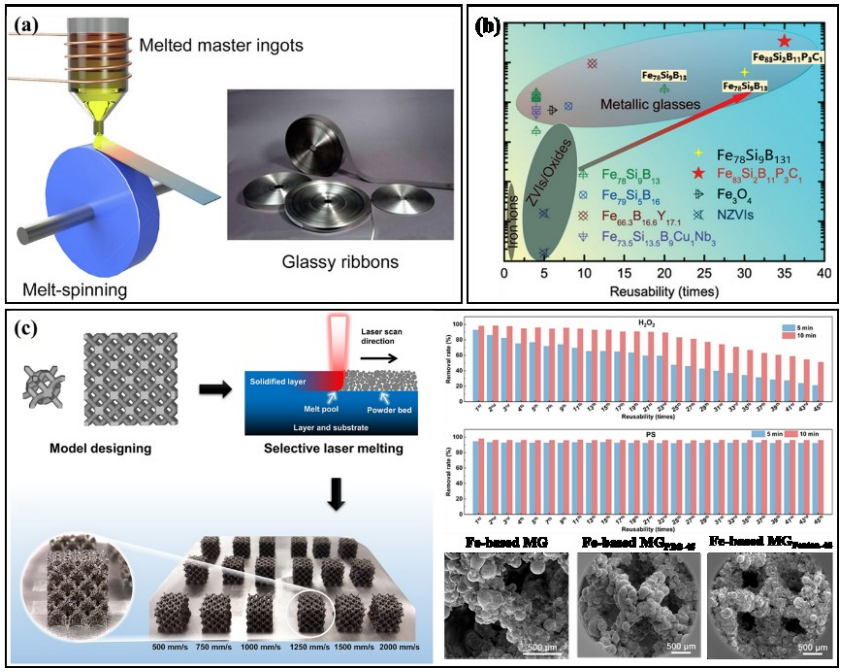

426

427 **Fig. 9.** Typical metallic glasses used in persulfate-AOPs: (a) schematic diagram of melt-spinning process
428 for manufacturing glassy ribbons and an optical photograph of typical product (reprinted with permission
429 from [57], copyright 2019 Elsevier); (b) comparison of the catalytic stability of different iron-based
430 materials (reprinted with permission from [64], copyright 2019 Wiley); and (c) synthetic procedure, SEM
431 images, and reusability of as-produced Fe-based MG matrix composite (Fe-based MG_{PDS-45}: the Fe-based
432 MG_{PDS-45} after 45-times use in PDS activation process; Fe-based $MG_{Fenton-45}$: the Fe-based MG_{PDS-45} after
433 45-times use in Fenton-like reaction process) (reprinted with permission from [60], copyright 2020
434 Elsevier).

435 Aerogels are a class of highly porous lightweight materials with an average pore
436 size in the tens of nanometers, and are sublimated from the liquid components of
437 traditional gels (usually by freeze-drying or critical point drying) [65, 66]. Cellulose
438 aerogels have wide application prospects due to their high specific surface area, uniform
439 pore size distribution, biodegradability, recyclability, and low cost [65, 67]. As
440 indicated in **Table 3**, ZIF-9 and ZIF-12 were decorated on cellulose aerogels with
441 macroscopic 3D structure and low weight (**Fig. 10(a)**), and the aerogels then used to
442 activate PMS effectively [68]. Carbon aerogels are a new class of carbonaceous

443 materials that feature an interconnected framework, possess large specific surface areas,
444 and have a hierarchical pore structure. Co-doped carbon aerogels (CoCA) activate PMS
445 at lower activation energy, effectively removing organic pollutants while maintaining a
446 low metal ion leaching rate [69] (**Table 3**). As evident in **Fig. 10(b)**, CoCA floats
447 beneath the surface of the aqueous solution and can be completely removed without
448 any change in form.

449 Flow-type configurations are suitable for continuous treatment of wastewater, thus
450 expanding the applicability of aerogels. However, traditional isotropic graphene
451 aerogels and foams contain randomly dispersed graphene sheets, which would cause
452 erosion and seriously reduce the flux. Compared with isotropic $CoFe_2O_4$@graphene
453 hybrid aerogels (CFO@GA-I), anisotropic $CoFe_2O_4$@graphene hybrid aerogels
454 (CFO@GA-A) have higher flux, lower metal ion leaching concentration, and much
455 better, stable catalytic performance (**Table 3** and **Fig. 10(c)**) [70]. Moreover, CFO@GA
456 aerogels can be stacked together to meet complex application conditions (**Fig. 10(d)**).

457 Hydrogels have rigid but soft elastic networks that permeate one another, giving
458 them higher mechanical strength and strain capacity than aerogels [71]. Among
459 hydrogels, hydrophilic material offers an appropriate support conducive to mass
460 transfer in water treatment, and which reduces the dissolution of metal ions [72].
461 Polyacrylic acid (PAA) is a kind of ionic hydrogel with polar carboxyl groups (-COOH)
462 that exhibit high adsorption efficiency toward metal ions and strong interaction with
463 water. After successfully synthesizing a 3D composite hydrogel based on
464 CoOOH/graphene oxide (CoOOH/GO) and PAA hydrogel precursor, Yi et al. [73]

constructed an automatic water treatment system under laboratory conditions (**Fig. 10(e)**). Duan et al. [74] discovered the formation of chemical bonds between Co_3O_4 and graphene in a 3D hierarchical Co_3O_4/graphene hydrogel composite with high specific surface area, stable structure, and significantly heterogeneous surface synergistic effect (**Table 3**). Later, the dual network hydrogel consisted of two interpenetrating networks with enhanced structural properties [75-77]. Meanwhile, Zhuang et al. [78] prepared a double-network hydrogel templated FeS/graphene (DMG) based on a double-network hydrogel containing Fe. This not only facilitated the formation of high-quality graphene at a low cost but also achieved intensive interactions between Fe and graphene, as shown in **Fig. 10(f)**.

Overall, immobilizing as-prepared nanocatalysts into hydrogel can reduce the leaching concentration of metal ions based on specific chemical bond formation, thus avoiding the loss of nanocatalysts from the reactor [78-80].

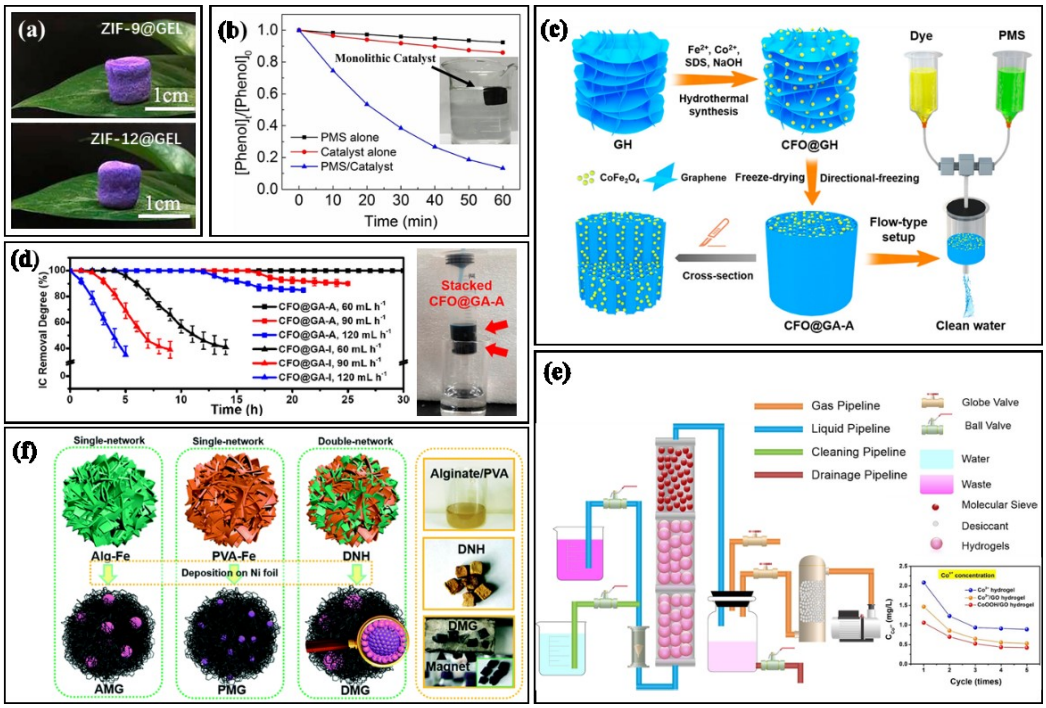

Fig. 10. Typical aerogels and hydrogels used in persulfate-AOPs: (a) photographs of ZIF-based hybrid

aerogels (reprinted with permission from [68], copyright 2018 Elsevier); (b) elimination of phenol under different conditions, and photographs of CoCA in water (inset) (reprinted with permission from [69], copyright 2020 Elsevier); (c) schematic illustration of the preparation of an anisotropic $CoFe_2O_4$@GA-A and its application for the continuing treatment of wastewater with a flow-type setup (reprinted with permission from [70], copyright 2020 Elsevier); (d) plots of removal efficiencies of organic pollutants for $CoFe_2O_4$@GA-A and $CoFe_2O_4$@GA-I at different flow rates, and a photograph of real-time catalytic experiments using $CoFe_2O_4$@GA-A and stacked $CoFe_2O_4$@GA-As (each red arrow indicates a piece of $CoFe_2O_4$@GA-A) (reprinted with permission from [70], copyright 2019 ACS); (e) schematic illustration of degradation equipment flowchart based on CoOOH/GO hydrogel composite (reprinted with permission from [73], copyright 2019 ACS); and (f) preparation routine and photographs of samples (reprinted with permission from [78], copyright 2020 RSC).

Apart from the abovementioned support materials, many other uncommon supports, such as polymer sponges [81], metal plates [82-85], and sand [86, 87], have been studied for the immobilization of persulfate catalysts, as listed in **Table 4**. These materials have two benefits: easy procurement in massive quantities and cost-efficiency for large-scale procedures.

Using a sponge catalyst composed of polyvinyl alcohol (PVA) as support, a chemically bonded Co_3O_4 nanoflower sponge (SP-50) was prepared with good mechanical and elastic properties, adjustable geometry, multi-porosity, and multi-dimensionality. As shown in **Fig. 11(a)**, the catalytic sponge floats on water and, more importantly, can be easily recycled. Due to the use of bonding materials or organic adhesives that limit contact between catalyst and target matrix, many published works concerning immobilized catalysts for persulfate activation have recently focused on direct *in situ* growth catalysts situated on metal plates. For instance, Hoffmann et al. [83] employed cobalt-doped Black TiO_2 nanotubes (Co-Black TNT) as PMS activators

505 to degrade organic pollutants (**Fig. 11(b)**). Moreover, stainless steel was used for cost-
506 effective bifunctional supports and catalysts after appropriate pretreatment, owing to its
507 mechanical firmness, corrosion resistance, conductivity, and ease of scale-up (**Fig.**
508 **11(c)**) [88]. In another study, waste from a sandwich cathode containing $LiMn_2O_4$ was
509 directly used as a catalyst to activate PMS for removal of organic pollutants in water,
510 which were then entirely (and easily) collected from the reaction system (**Fig. 11(d)**)
511 [84].

512 As previously remarked, the continuous flow reactor system has two notable
513 characteristics: ease of operation and low energy consumption, thus marking a
514 milestone in the practical use of AOPs. Considering pollutant removal performance and
515 operation process cost (see **Table 4**), $CoFe_2O_4$ was placed onto a quartz sand support
516 ($CoFe_2O_4$-QS) and packed into a column reactor to activate PMS [86]. Similarly, a
517 systematic study evaluated the feasibility of using a sand column reactor, consisting of
518 BFMO (i.e., $Mn_{1.5}FeO_{6.35}$) and sand, to activate PMS *in situ* for the treatment of
519 trichloroethylene-contaminated water (**Fig. 11(e)**) [87]. The current findings indicate
520 that BFMO is a very stable and long-acting catalyst for persulfate-based *in situ* chemical
521 oxidation (ISCO), which may be employed for groundwater remediation.

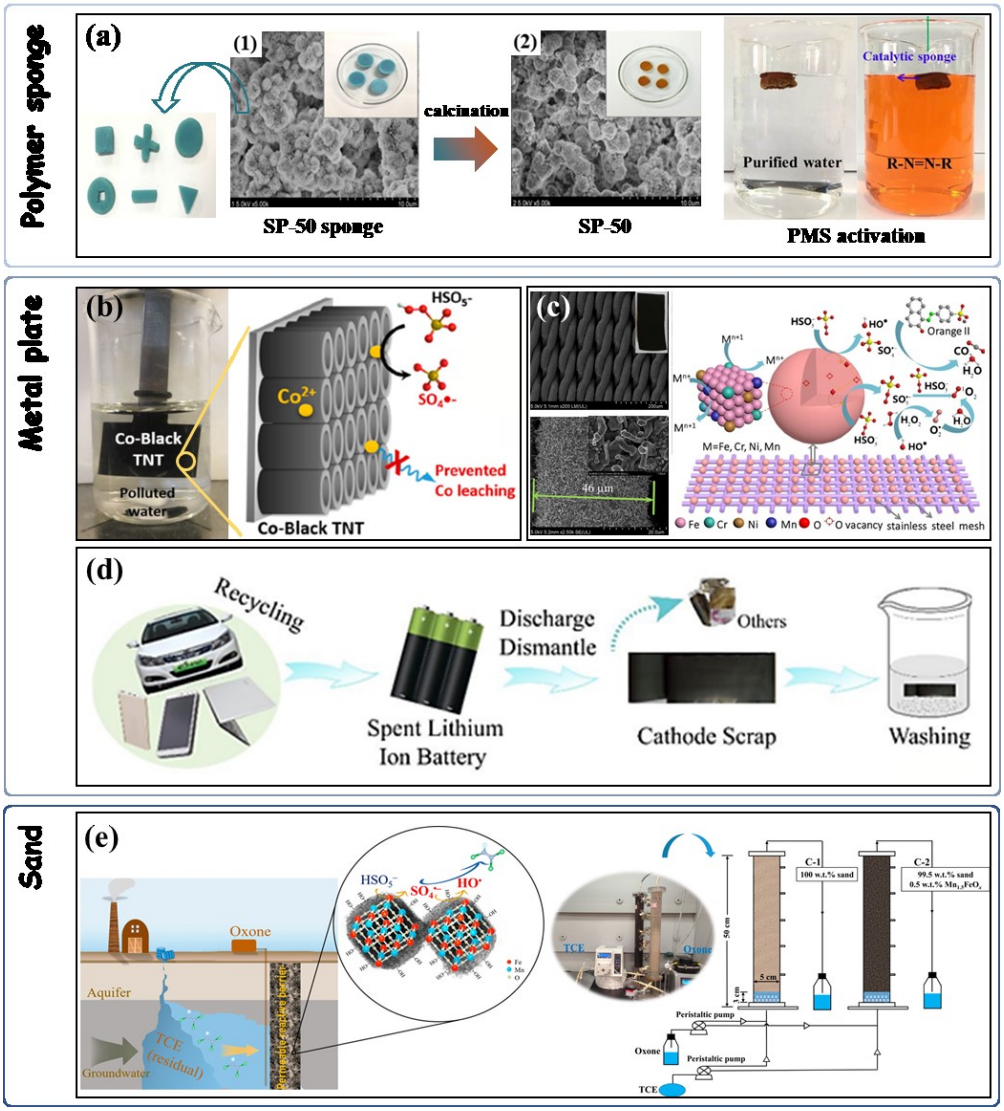

Fig. 11. Specific materials based on uncommon supports prepared for persulfate activation: (a) digital images of as-obtained SP-50 sponge cut into different geometrical shapes; SEM images of (1) SP-50 sponge and (2) SP-50; digital photograph of SP-50/PMS reactive process (reprinted with permission from [81], copyright 2019 Wiley); (b) digital photograph of Co-Black TNT/PMS reactive process and the activation mechanisms (reprinted with permission from [83], copyright 2019 ACS); (c) SEM images and activation mechanisms of the stainless-steel/PMS system for degrading organic contaminants (reprinted with permission from [85], copyright 2020 Elsevier); (d) recycling process of spent lithium-ion battery (reprinted with permission from [84], copyright 2020 ACS); and (e) schematic illustration of PMS-based *in situ* chemical oxidation process and the sand columns (5 cm internal diameter × 50 cm length) working mode (reprinted with permission from [87], copyright 2020 ACS).

4. Electrocatalytic auxiliary systems

Electrocatalytic treatment is conducted by applying a potential to the anode and cathode in a reactor. In this process, influent is used as the electrolyte, with chemicals added as necessary to improve conductivity. Direct degradation of targeted pollutants occurs through charge transfer on the electrode surface. Anode and cathode processes can also indirectly promote the removal of pollutants through reaction with electrochemically generated ROS. Construction of an electrochemically-activated persulfate process can be achieved by means of a sacrificial anode system, electric filtration system, and photoelectrocatalytic system, as shown in **Fig. 2**. These reaction systems improve degradation efficiency while reducing power consumption and cost. They are particularly applicable to decentralized processes because of their efficiency and stability at small scale and ease of automatic control by current/voltage adjustment.

Electrochemical systems with addition of iron ions (Fe^{2+} or Fe^{3+}) for persulfate activation were initially implemented to remove organic pollutants [89-91]. It was found unexpectedly that Fe^{2+} can regenerate from the cathodic reduction reaction in Fered-Fenton and other electro-Fenton processes [89], thereby overcoming the problem of Fe^{2+} regeneration after transformation to Fe^{3+}. Thus, the reaction systems could possess continuous persulfate catalytic capability; however, a large amount of iron sludge would inevitably be produced.

Later, electrochemical enhancement of persulfate-AOPs, with iron sheets used as sacrificial anodes, was used to promote destruction of organic contaminants (**Table 5**). In the oxidation process, once a current was applied between the anode and cathode, a

predetermined amount of persulfate was then added to the reactor. Ferrous ions produced by sacrificial iron anodes mediated the persulfate decomposition. In **Fig. 2**, the production rate of Fe^{2+} is controlled by the positive current of the iron anode, according to the reaction expressed by Eq. (1). Consumed Fe^{2+} is regenerated on the cathode, satisfying Eq. (2). In turn, OH^- forms and may restore the pH value and redox potential, thus inhibiting heavy metals from leaching into the subsurface, as expressed by Eq. (3). Therefore, the iron electrode can be readily introduced into a polluted region to control persulfate activation *in situ*, thus minimizing the potential loss of persulfate during injection and transportation [92].

$$Fe - 2e^- \rightarrow Fe^{2+} \quad (1)$$

$$Fe^{3+} + 2e^- \rightarrow Fe^{2+} \quad (2)$$

$$2H_2O + 2e^- \rightarrow H_2 + OH^- \quad (3)$$

This sacrificial anode reaction system has several important advantages: low cost, substantially reduced energy consumption, and remarkably increased pollutant degradation. However, the approach has been criticized due to the increased operating cost incurred from disposal of the iron sludge byproduct [93, 94]. Song et al. [95] detected the electrochemical activation of PDS at the Ti/Pt anode, whereas Farhat et al. [96] studied the PDS activation performance of a boron-doped diamond electrode. From the foregoing, it was found that discharge is the dominant factor in the electrochemical activation processes of PDS, which induces the generation of the PDS transition state. Hence, the electrode only plays a role in electron transfer and does not directly participate in persulfate activation.

In capacitive deionization (CDI), application of a direct current voltage that is lower than the water breakdown voltage (1.23 V) on the porous electrode can induce ions or charged organic groups in an aqueous solution to gather quickly on the surface of the polarized electrode and attract oppositely charged species to their surfaces; this phenomenon is called the illegal Larch process [97]. Due to their great conductivity, large specific surface area, and chemical stability, CNTs have been widely used as electrode materials for CDI to remove organic pollutants from wastewater [93, 98]. As reported, multi-walled carbon nanotube (MWCNT) cathodes were synthesized by a casting method using PVA as binder and graphite sheet as support [93]. As shown in **Fig. 12(a)**, during each operation, a certain amount of stock liquid was continuously pumped into the cell by a peristaltic pump until the discharged liquid returned to the electrochemical cell. Interaction between persulfate and carbon surface functional groups has been found to play a remarkable role in persulfate-AOPs. Electrochemical reactions usually occur on the electrode surface, and the generated free radicals are usually adsorbed on the electrode surface, although they are difficult to disperse thoroughly in the bulk solution [95]. However, as shown in **Fig. 12(b)**, activation and electro-adsorption of PDS on the surface of a porous carbon electrode can promote electron transfer between the generated active substance and target pollutant, which is conducive to the degradation of pollutants. Correspondingly, the MWCNT electrode reduces the working voltage and enhances PDS activation performance to degrade organic pollutants simultaneously. The results showed that organic compounds on the electrode surface and the generated reaction species helped promote the electron

transfer progress through the synergistic effect of electro-adsorption of pollutants and electrochemical activation of PDS.

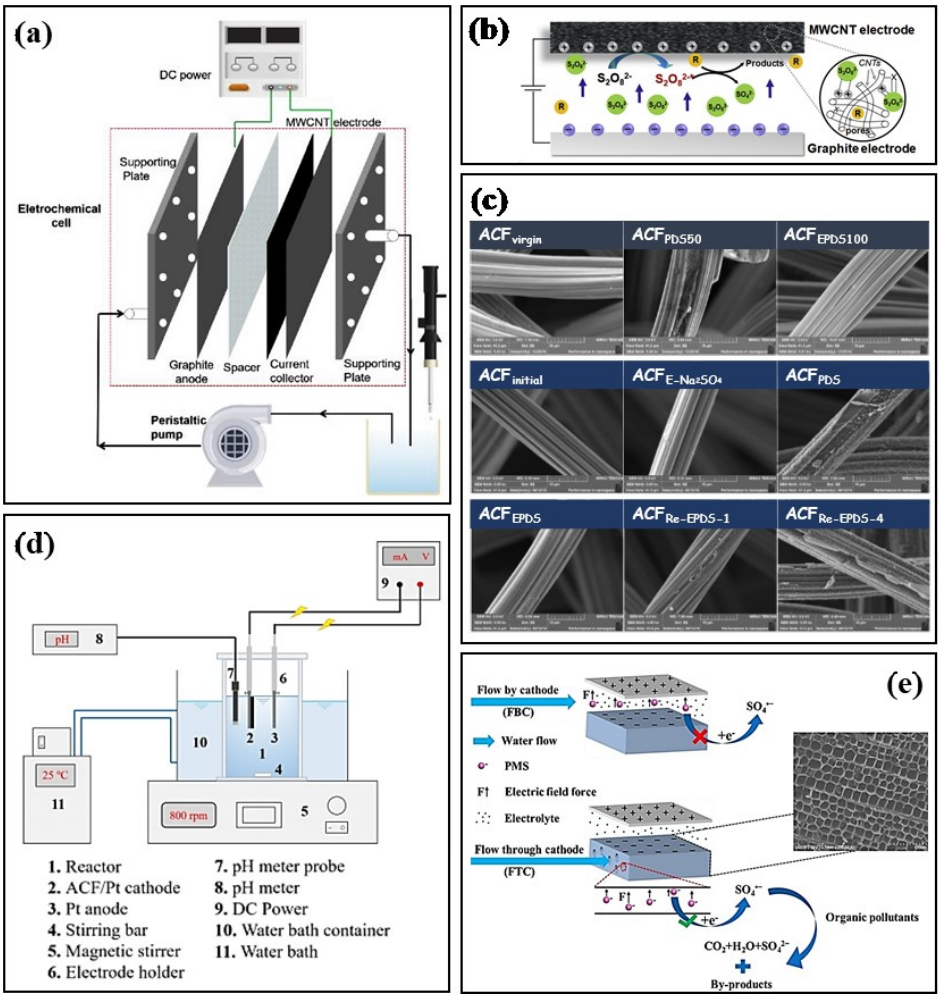

Fig. 12. Electrocatalytic auxiliary systems constructed for persulfate activation: (a) schematic diagram of electrochemical activation of PDS and aniline degradation experiment (reprinted with permission from [93], Copyright 2018 Elsevier); (b) proposed mechanism of organic pollutant removal by asymmetric quasi capacitive deionization (AQCDI)/PDS/1.2V system (R represents the organic molecule and X represents the active sites in MWCNTs) (reprinted with permission from [98], copyright 2019 Elsevier); (c) SEM images of the ACF in different reaction systems (reprinted with permission from [99, 100], copyright 2018 and 2020 Elsevier); (d) schematic representation of ACF Regeneration experimental setup (reprinted with permission from [101], copyright 2020 ACS); and (e) schematic diagram of the E-PMS activation mechanism via FTC and FBC strategy (reprinted with permission from [102], copyright 2020 ACS).

Likewise, Han et al. [103] investigated an enhanced electric activated carbon fiber

(ACF)/ferric iron/PDS (ACF-E/Fe^{3+}/PDS) process in which ACF served as a cathode. The results showed that the ACF cathode did not play a substantial role in activating PDS, and a large number of iron ions were deposited on the cathode surface, indicating good adsorption performance. Liu et al. [100] investigated the influence of operational conditions, including pH, electrode potential temperature, peroxydisulfate concentration, and water matrix. As listed in **Table 5**, ACF-E/PDS achieved a high pollutant removal rate of 98.78% in 30 min with high PDS concentration [103], proving that sufficient PDS can efficiently and quickly degrade pollutants. Therefore, in the ACF-E/PDS system, the economic benefits and environmental effects of PDS consumption or iron sludge disposal require further research. As depicted in **Fig. 12(c)**, SEM images of ACF_{virgin} (virgin ACF) and $ACF_{EPDS100}$ (electro PDS (E-PDS) reacted ACF after reutilization of 100 times) presented relatively neat surfaces, except that PDS oxidation caused the surface of ACF_{PDS50} to become cracked and rough (the case corresponding to PDS reacted ACF after 50-times reutilization). This finding may be attributed to electrons on the cathode reducing damage by ROS or PDS to ACF while maintaining continuous generation of $SO_4^{\bullet-}$ without depleting the electron supply residues of ACF. Furthermore (see **Table 5**), addition of PMS evidently improved the current in the $MnFe_2O_4$/carbon fiber paper (CFP) electrode [104] as well as in the PDA/CF cathode [105], indicating that the reaction between PMS and $MnFe_2O_4$/CFP or PDA/CF was energetically favorable. Moreover, the applied bias and photogenerated electrons of the photoanode facilitated the formation of different valence state ions in $MnFe_2O_4$, which activated PMS for $SO_4^{\bullet-}$ induction and catalytic stability of the

635 $MnFe_2O_4$/CFP cathode [104].

636 This kind of cathodic catalyst protection phenomenon also exists in cathodic
637 material regeneration, such as the *in situ* regeneration of phenol-saturated ACF by an
638 electro-PDS process [99]. The surface of ACF_{PDS} (virgin ACF immersed in the PDS
639 system for 180 min) was attacked and became covered with a mass of attachments
640 because ACF acted as a catalyst rather than an initiator. Compared with ACF_{PDS}, the
641 morphological characteristics and pore texture ACF_{EPDS} (virgin ACF immersed in PDS
642 with 1 A current applied for 180 min) and $ACF_{initial}$ coincided, such that the pore
643 remained almost unchanged.

644 By comparison with conventional electrochemical regeneration, the E-PDS
645 process can regenerate exhausted ACF and mineralized desorption pollutants
646 simultaneously by activating PDS with much lower energy consumption (1/6).
647 However, a large number of oxides and oligomers produced by anodic oxidation can be
648 re-adsorbed to carbon, resulting in a regeneration efficiency of only about 60%. What
649 is worse is that, compared with $ACF_{Re\text{-}E\text{-}PDS\text{-}1}$ (phenol-saturated ACF regenerated in the
650 E-PDS process for one cycle), the structure of $ACF_{Re\text{-}E\text{-}PDS\text{-}4}$ (phenol-saturated ACF
651 regenerated in E-PDS process for four cycles) deteriorated severely, as shown in the
652 SEM image in **Fig. 12(d)**. Therefore, after undergoing regeneration four times, the
653 regeneration efficiency decreased to less than 40%. As reported, the electro-PMS (E-
654 PMS) treatment progress is more suitable for the regeneration of activated carbon [101].
655 Phenol-saturated activated CF was regenerated *in situ* using an electro PMS reaction
656 system, as shown in **Fig. 12(d)**. This reaction system mineralized the desorbed

contaminants (81.90%) while consuming only one-tenth of the energy. Even after ten cycles, regeneration remained effective at around 60% of the initial value, and cathodic polarization during E-PMS regeneration effectively protected the physical structure and chemical properties of ACF. Nevertheless, ACF had a minor impact on PMS self-decomposition, and its role in E-PMS was distinct from that of the E-PDS process. Therefore, there is an urgent need to conduct more systematic, deeper studies on the performance, experimental setup, and reaction mechanisms of combined electrochemical and persulfate activation, which is considered a sustainable, efficient, low-toxicity technique for the remediation of contaminated water.

Several studies have activated persulfate on a plate cathodic surface, but achieved poor performance (see e.g. Zhang et al. [102]). Electrostatic repulsion tends to drive persulfate anions away from the cathode because both anions and cathode are negatively charged. Given the poor breakdown of persulfate and the low creation of radicals, the contaminants then degrade slowly. Two possible approaches to overcoming this problem are to shorten the diffusion distance and to increase collision and contact between persulfate anions and the cathode. Zhang et al. used carbonized wood with well-ordered channels as the cathode (**Table 5**), and performed a set of comparative experiments for a flow-by cathode (FBC) and a flow-through cathode (FTC) (**Fig. 12(e)**) to confirm that the microchannels of the FTC could boost the creation of radicals, and organics degradation. Cycling tests revealed that this FTC was quite stable. As a result, activating persulfate in FTC is an effective technique for increasing radical yield and availability.

The electro-activated persulfate process mainly involves an electron transfer reaction. Increases in current density and residence time tend to improve the number of electrons transferred and enhance the efficiency of the electrochemical activation. Several issues remain unresolved for all electrochemical–persulfate reaction systems. Future research should consider energy consumption, electrode manufacturing costs, power consumption, persulfate consumption, and loss in treatment capacity. Future research should also consider how to avoid secondary pollution by excess PMS and its associated reaction products, and how to recycle principal byproducts such as SO_4^{2-}. Furthermore, such studies should not only be conducted in the laboratory but also expanded to pilot scale.

5. Challenges and outlook

The integration of various conventional research disciplines, such as materials science for the creation of purpose-driven catalysts and water treatment engineering for the construction of practical reactors, has led to the effective application of nanoparticle-based AOPs for water remediation. Correspondingly, rapid advances have been achieved over the past few years in the emerging field of persulfate-based immobilized-catalyst systems. This review article summarizes current developments concerning nanocatalyst immobilization in persulfate-AOPs for target contaminant removal. Various immobilization techniques onto supports, including membrane-based reaction systems (immersion mode, filtration mode), electrocatalytic auxiliary systems, and other supports (metallic glasses, aerogels, and hydrogels, or specific materials), are

discussed.

Compared with common nanocatalyst reaction systems, the immobilized-catalyst system can bypass the separation problem to reduce scour and prevent aggregation by anchoring nanoparticles onto porous or large-particle carriers. As a result, great effort has been devoted to exploring suitable support substances for nanocatalysts and designing reactors that cope with the changing environment for targeted pollutant removal. Meanwhile, a series of studies have been carried out to gain insight into the persulfate activation mechanism. Even so, considerable challenges remain regarding high-performance reactors and the practical applications of persulfate-based AOPs.

To ensure excellent activation performance and high reusability of next-generation multifunctional treatment systems, it is necessary to develop advanced reactors, incorporating advances in materials science and a fundamental understanding of key mechanisms. For example, direct evidence is still lacking for the outer- and inner-sphere connection between nanocatalysts and supporting materials. Meanwhile, interactions remain uncertain among catalysts, persulfate, and targeted pollutants. Although laboratory studies have been undertaken to develop immobilized catalysts with simple recycling operation and excellent catalytic performance, the application and commercialization of such technology is quite low in more complicated situations. Future studies are expected to employ persulfate-AOPs at pilot and semi-industrial scales with the goal of reactor design and the focus on engineering issues.

In terms of the prospects for persulfate-based immobilized-catalyst systems, we propose the following foci:

(1) *Determine a universal design principle by which to optimize the structure and catalytic performance of heterogeneous catalysts.* In practice, the optimization of electronic characteristics and elemental composition of nanoparticles plays a remarkable role in catalytic processes. Through careful material design and theoretical calculations, it is possible to prepare a catalyst with amazing performance. Furthermore, reaction active sites and reaction pathways to the catalyst can be fully understood. Theoretical calculation and *in situ* characterization are two powerful techniques to advance reaction mechanisms, both of which are instructive in determining design and preparation rules for high-performance materials. Moreover, many state-of-the-art nanoparticles are notable for environmental applications, but have yet to make a significant impact in the field of water treatment. Covalent organic frameworks (COFs), for example, are an attractive new form of porous organic nanomaterials with desirable properties, including a completely organic metal-free backbone, low mass density, well-defined topology, structural variety, high heat resistance, and permanent porosity. An effective, facile method for fabricating flexible, free-standing pure COF membranes has been described in a previous study, thus allowing development of new forms of membrane-based persulfate-AOPs [106]. Furthermore, based on the mononuclear nature of the catalytic site, single-atom catalysts possess superior atomic utilization efficiency, thus inheriting the advantages of homogeneous and heterogeneous catalysts.

(2) *Optimize the combination of active materials and supporting substances.* The catalyst preparation stage pertains to reactor design and systems engineering. Here the activity and stability of catalysts are only two of the key factors. The goal is to improve

744 the effective utilization of persulfate-AOPs. In most cases, immobilized-catalyst
745 systems are inherently mass transfer-limited. Correspondingly, the approach is based
746 on nanocatalysts with outstanding, stable catalytic capability, which exploit the
747 maximized surface area of the nanoscale active material and the support material
748 architecture. Additional studies should thus reveal the relationship between the
749 excellent catalytic performance of nanocatalysts and the structural properties of their
750 supports in order to guide reactor design in systems engineering. Given their
751 widespread applications, the as-expected immobilized catalysts must be manufactured
752 at industrial scale (in tons), resulting in a stable, mature market. All the foregoing
753 advances, including catalytic performance, stability, flexibility, and cost-efficiency, are
754 aimed at the development of new reactors.

755 (3) *Solve problems of decreased performance in various complex water matrices*
756 *and formation of reaction byproducts.* Most of the studies examined in this review
757 detected the removal effect of target pollutants using synthetic water to evaluate the
758 catalytic capability of catalysts, hence, the lack of background organic content.
759 However, due to competitive adsorption onto catalyst surfaces and radical scavenging
760 in an aqueous solution, natural organic matter (NOM) is commonly recognized to
761 reduce persulfate-AOP performance. The remarkable spatiotemporal changes that take
762 place in water quality parameters (e.g. target pollutant concentration, turbidity, various
763 coexisting ions, and pH) are inherent challenges that have often been overlooked at
764 laboratory scale. Despite efforts to recreate realistic settings, the absence of defined
765 experimental methodology has made it difficult to obtain a quantitative evaluation of

766 the actual processing effect of persulfate-AOPs. In turn, this has limited effective
767 technology transfer and commercialization. It should be noted that the majority of the
768 research reviewed herein focused on the degradation of single or a few types of
769 pollutants. In actual sewage, many types of pollutants co-exist, and so the cooperative
770 inhibition of different types of pollutants merits further in-depth research. Hence, future
771 studies are expected to employ persulfate-AOPs at pilot- and semi-industrial scales,
772 aimed at improved reactor design while focusing on engineering aspects.

773 (4) *Reasonable evaluation of treatment effect of the reaction system*. Much work
774 has yet to be done in properly assessing the viability and industrialization of
775 immobilized catalysts in terms of cost and life-cycle impacts (which are mostly
776 unpredictable and unclear at this early stage of research). Although new studies on
777 persulfate-based AOPs for water treatment are often reported nowadays, these
778 numerous studies and proposed technology combinations pose great challenges for the
779 assessment of AOPs. The challenges include operating costs (e.g., energy consumption,
780 and chemical inputs), general practicality (e.g., physical footprint, oxidation byproduct
781 production, and impact on multiple microbial subsistence), and sustainability (e.g.,
782 resource use, and carbon footprint). Future studies are likely to confirm the economic
783 benefits and environmental consequences of persulfate-based AOPs. For this purpose,
784 life-cycle analysis is required, which involves evaluating energy usage, natural
785 resources, and chemical products related to emissions to air, soil, and water, as well as
786 considering potential trade-offs in actual environmental remediation.

787

Declaration of Interest Statement

The authors declare that they have no known competing financial interests or personal relationships that could have appeared to influence the work reported in this paper.

Acknowledgements

This work was funded by the National Natural Science Foundation of China (Grant No. 42177382).

References

[1] S.V. Bhide, S.B. Grant, E.A. Parker, M.A. Rippy, A.N. Godrej, S. Kaushal, G. Prelewicz, N. Saji, S. Curtis, P. Vikesland, A. Maile-Moskowitz, M. Edwards, K.G. Lopez, T.A. Birkland, T. Schenk, Addressing the contribution of indirect potable reuse to inland freshwater salinization, Nat. Sustain. 4 (2021) 699-707.

[2] P.J.J. Alvarez, C.K. Chan, M. Elimelech, N.J. Halas, D. Villagrán, Emerging opportunities for nanotechnology to enhance water security, Nat. Nanotechnol. 13 (2018) 634-641.

[3] H. Sun, Q. Zhang, R. Wang, H. Wang, Y.T. Wong, M. Wang, Q. Hao, A. Yan, R.Y.T. Kao, P.L. Ho, H. Li, Resensitizing carbapenem- and colistin-resistant bacteria to antibiotics using auranofin, Nat. Commun. 11 (2020) 5263.

[4] R. Wang, T.P. Lai, P. Gao, H. Zhang, P.L. Ho, P.C.Y. Woo, G. Ma, R.Y.T. Kao, H. Li, H. Sun, Bismuth antimicrobial drugs serve as broad-spectrum metallo-β-lactamase inhibitors, Nat. Commun. 9 (2018) 439.

[5] C. Munck, M. Albertsen, A. Telke, M. Ellabaan, P.H. Nielsen, M.O.A. Sommer, Limited dissemination of the wastewater treatment plant core resistome, Nat. Commun. 6 (2015) 8452.

[6] R. Das, C.D. Vecitis, A. Schulze, B. Cao, A.F. Ismail, X. Lu, J. Chen, S. Ramakrishna, Recent advances in nanomaterials for water protection and monitoring, Chem. Soc. Rev. 46 (2017) 6946-7020.

[7] P. Zhou, W. Ren, G. Nie, X. Li, X. Duan, Y. Zhang, S. Wang, Fast and long-lasting

iron(III) reduction by boron toward green and accelerated Fenton chemistry, Angew. Chem. Int. Ed. 59 (2020) 16517-16526.
[8] C. Vilchèze, T. Hartman, B. Weinrick, W.R. Jacobs, Mycobacterium tuberculosis is extraordinarily sensitive to killing by a vitamin C-induced Fenton reaction, Nat. Commun. 4 (2013) 1881.
[9] R. Xiao, T. Ye, Z. Wei, S. Luo, Z. Yang, R. Spinney, Quantitative structure-activity relationship (QSAR) for the oxidation of trace organic contaminants by sulfate radical, Environ. Sci. Technol. 49 (2015) 13394-13402.
[10] D. Gu, C. Guo, S. Hou, J. Lv, Y. Zhang, Q. Feng, Y. Zhang, J. Xu, Kinetic and mechanistic investigation on the decomposition of ketamine by UV-254 nm activated persulfate, Chem. Eng. J. 370 (2019) 19-26.
[11] C. Chen, Y. Du, Y. Zhou, Q. Wu, S. Zheng, J. Fang, Formation of nitro(so) and chlorinated products and toxicity alteration during the UV/monochloramine treatment of phenol, Water Res. 194 (2021) 116914.
[12] Y. Lei, X. Lei, P. Westerhoff, X. Zhang, X. Yang, Reactivity of chlorine radicals (Cl• and $Cl_2^{\bullet-}$) with dissolved organic matter and the formation of chlorinated byproducts, Environ. Sci. Technol. 55 (2021) 689-699.
[13] J.M. Barazesh, C. Prasse, D.L. Sedlak, Electrochemical transformation of trace organic contaminants in the presence of halide and carbonate ions, Environ. Sci. Technol. 50 (2016) 10143-10152.
[14] P. Avetta, A. Pensato, M. Minella, M. Malandrino, V. Maurino, C. Minero, K. Hanna, D. Vione, Activation of persulfate by irradiated magnetite: implications for the degradation of phenol under heterogeneous photo-Fenton-like conditions, Environ. Sci. Technol. 49 (2015) 1043-1050.
[15] R. Guo, Q. Meng, H. Zhang, X. Zhang, B. Li, Q. Cheng, X. Cheng, Construction of Fe_2O_3/Co_3O_4/exfoliated graphite composite and its high efficient treatment of landfill leachate by activation of potassium persulfate, Chem. Eng. J. 355 (2019) 952-962.
[16] R. Guo, Y. Wang, J. Li, X. Cheng, D.D. Dionysiou, Sulfamethoxazole degradation by visible light assisted peroxymonosulfate process based on nanohybrid manganese dioxide incorporating ferric oxide, Appl. Catal. B: Environ. 278 (2020) 119297.
[17] B.C. Hodges, E.L. Cates, J.H. Kim, Challenges and prospects of advanced oxidation water treatment processes using catalytic nanomaterials, Nat. Nanotechnol. 13 (2018) 642-650.
[18] F. Xia, Y. Yang, S. Wan, P. Gao, X. Han, Y. Jiang, X. Xu, Influence of pre-treatment on remediation of nitrobenzene contaminated groundwater by combined oxidation-reduction techniques, Res. Environ. Sci. 33 (2020) 2001-2010.
[19] K.R. Zodrow, Q. Li, R.M. Buono, W. Chen, G. Daigger, L. Dueñas-Osorio, M. Elimelech, X. Huang, G. Jiang, J.H. Kim, B.E. Logan, D.L. Sedlak, P. Westerhoff, P.J.J. Alvarez, Advanced materials, technologies, and complex systems analyses: emerging

opportunities to enhance urban water security, Environ. Sci. Technol. 51 (2017) 10274-10281.
[20] Y. Chen, G. Zhang, H. Liu, J. Qu, Confining free radicals in close vicinity to contaminants enables ultrafast Fenton-like processes in the interspacing of MoS_2 membranes, Angew. Chem. Int. Ed. 58 (2019) 8134-8138.
[21] A. Cruz-Alcalde, N. López-Vinent, R.S. Ribeiro, J. Giménez, C. Sans, A.M.T. Silva, Persulfate activation by reduced graphene oxide membranes: practical and mechanistic insights concerning organic pollutants abatement, Chem. Eng. J. 427 (2022) 130994.
[22] D. Zhao, A. Armutlulu, Q. Chen, R. Xie, Enhanced ciprofloxacin degradation by electrochemical activation of persulfate using iron decorated carbon membrane cathode: promoting direct single electron transfer to produce $^1O_2$, Chem. Eng. J. 437 (2022) 135264.
[23] O. Vieira, R.S. Ribeiro, M. Pedrosa, A.R. Lado Ribeiro, A.M.T. Silva, Nitrogen-doped reduced graphene oxide-PVDF nanocomposite membrane for persulfate activation and degradation of water organic micropollutants, Chem. Eng. J. 402 (2020) 126117.
[24] R. Guo, Y. Chen, L.C. Nengzi, L. Meng, Q. Song, J. Gou, X. Cheng, *In situ* preparation of carbon-based Cu-Fe oxide nanoparticles from CuFe Prussian blue analogues for the photo-assisted heterogeneous peroxymonosulfate activation process to remove lomefloxacin, Chem. Eng. J. 398 (2020) 125556.
[25] H. Li, L. Yang, L. He, Y. Ma, X. Yan, L. Wu, Z. Zhang, Kinetics and mechanisms of chloramphenicol degradation in aqueous solutions using heat-assisted nZVI activation of persulfate, J. Mol. Liq. 313 (2020) 113511.
[26] Y. Bao, Y.S. Tay, T.T. Lim, R. Wang, R.D. Webster, X. Hu, Polyacrylonitrile (PAN)-induced carbon membrane with *in-situ* encapsulated cobalt crystal for hybrid peroxymonosulfate oxidation-filtration process: preparation, characterization and performance evaluation, Chem. Eng. J. 373 (2019) 425-436.
[27] R. Guo, Y. Li, Y. Chen, Y. Liu, B. Niu, J. Gou, X. Cheng, Efficient degradation of sulfamethoxazole by CoCu LDH composite membrane activating peroxymonosulfate with decreased metal ion leaching, Chem. Eng. J. 417 (2021) 127887.
[28] Y. Yao, C. Lian, Y. Hu, J. Zhang, M. Gao, Y. Zhang, S. Wang, Heteroatoms doped metal iron-polyvinylidene fluoride (PVDF) membrane for enhancing oxidation of organic contaminants, J. Hazard. Mater. 338 (2017) 265-275.
[29] S. Yang, X. Qiu, P. Jin, M. Dzakpasu, X.C. Wang, Q. Zhang, L. Zhang, L. Yang, D. Ding, W. Wang, K. Wu, MOF-templated synthesis of $CoFe_2O_4$ nanocrystals and its coupling with peroxymonosulfate for degradation of bisphenol A, Chem. Eng. J. 353 (2018) 329-339.
[30] R. Guo, L.C. Nengzi, Y. Chen, Y. Li, X. Zhang, X. Cheng, Efficient degradation of

sulfamethoxazole by CuCo LDH and LDH@fibers composite membrane activating peroxymonosulfate, Chem. Eng. J. 398 (2020) 125676.
[31] O. Nechyporchuk, M.N. Belgacem, J. Bras, Production of cellulose nanofibrils: a review of recent advances, Ind. Crops Prod. 93 (2016) 2-25.
[32] C. Hou, W. Chen, L. Fu, S. Zhang, C. Liang, Y. Wang, Facile synthesis of a Co/Fe bi-MOFs/CNF membrane nanocomposite and its application in the degradation of tetrabromobisphenol A, Carbohydr. Polym. 247 (2020) 116731.
[33] N. Amiralian, M. Mustapic, S.A. Hossain, C. Wang, M. Konarova, J. Tang, J. Na, A. Khan, A. Rowan, Magnetic nanocellulose: a potential material for removal of dye from water, J. Haz. Mat. 394 (2020) 122571.
[34] Y. Dzenis, Structural nanocomposites, Science 319 (2008) 419-420.
[35] D. Papkov, N. Delpouve, L. Delbreilh, S. Araujo, T. Stockdale, S. Mamedov, K. Maleckis, Y. Zou, M.N. Andalib, E. Dargent, V.P. Dravid, M.V. Holt, C. Pellerin, Y.A. Dzenis, Quantifying polymer chain orientation in strong and tough nanofibers with low crystallinity: toward next generation nanostructured superfibers, ACS Nano 13 (2019) 4893-4927.
[36] R. Sridhar, R. Lakshminarayanan, K. Madhaiyan, V. Amutha Barathi, K.H.C. Lim, S. Ramakrishna, Electrosprayed nanoparticles and electrospun nanofibers based on natural materials: applications in tissue regeneration, drug delivery and pharmaceuticals, Chem. Soc. Rev. 44 (2015) 790-814.
[37] Y. Lei, Q. Wang, S. Peng, S. Ramakrishna, D. Zhang, K. Zhou, Electrospun inorganic nanofibers for oxygen electrocatalysis: design, fabrication, and progress, Adv. Energy Mater. 10 (2020) 1902115.
[38] Z. Zhu, Y. Xu, B. Qi, G. Zeng, P. Wu, G. Liu, W. Wang, F. Cui, Y. Sun, Adsorption-intensified degradation of organic pollutants over bifunctional α-Fe@carbon nanofibres, Environ. Sci.: Nano 4 (2017) 302-306.
[39] H. Shan, X. Dong, X. Cheng, Y. Si, J. Yu, B. Ding, Highly flexible, mesoporous structured, and metallic Cu-doped C/SiO_2 nanofibrous membranes for efficient catalytic oxidative elimination of antibiotic pollutants, Nanoscale 11 (2019) 14844-14856.
[40] W. Tian, H. Zhang, X. Duan, H. Sun, M.O. Tade, H.M. Ang, S. Wang, Nitrogen- and sulfur-codoped hierarchically porous carbon for adsorptive and oxidative removal of pharmaceutical contaminants, ACS Appl. Mater. Interfaces 8 (2016) 7184-7193.
[41] Y. Wang, S. Zhao, W. Fan, Y. Tian, X. Zhao, The synthesis of novel Co–Al_2O_3 nanofibrous membranes with efficient activation of peroxymonosulfate for bisphenol A degradation, Environ. Sci.: Nano 5 (2018) 1933-1942.
[42] Y. Wang, S. Hui, S. Zhan, R. Djellabi, J. Li, X. Zhao, Activation of peroxymonosulfate by novel Pt/Al_2O_3 membranes via a nonradical mechanism for efficient degradation of electron-rich aromatic pollutants, Chem. Eng. J. 381 (2020)

122563.
[43] T. Ma, L. Liu, B. Meng, J. Gao, S. Wang, S. Liu, Heterogeneous activation of peroxymonosulfate via a Ag-$La_{0.8}Ca_{0.2}Fe_{0.94}O_{3-\delta}$ perovskite hollow fibre membrane reactor for dye degradation, Sep. Purif. Technol. 211 (2019) 298-302.
[44] Y. Yao, H. Chen, J. Qin, G. Wu, C. Lian, J. Zhang, S. Wang, Iron encapsulated in boron and nitrogen codoped carbon nanotubes as synergistic catalysts for Fenton-like reaction, Water Res. 101 (2016) 281-291.
[45] C. Chu, J. Yang, X. Zhou, D. Huang, H. Qi, S. Weon, J. Li, M. Elimelech, A. Wang, J.H. Kim, Cobalt single atoms on tetrapyridomacrocyclic support for efficient peroxymonosulfate activation, Environ. Sci. Technol. 55 (2021) 1242-1250.
[46] C. Wang, P. Cheng, Y. Yao, Y. Yamauchi, X. Yan, J. Li, J. Na, *In-situ* fabrication of nanoarchitectured MOF filter for water purification, J. Hazard. Mater. 392 (2020) 122164.
[47] M. Pedrosa, G. Drazic, P.B. Tavares, J.L. Figueiredo, A.M.T. Silva, Metal-free graphene-based catalytic membrane for degradation of organic contaminants by persulfate activation, Chem. Eng. J. 369 (2019) 223-232.
[48] K. Yang, X. Zhu, B. Chen, Facile fabrication of freestanding all-carbon activated carbon membranes for high-performance and universal pollutant management, J. Mater. Chem. A 5 (2017) 20316-20326.
[49] X. Fan, S. Li, M. Sun, C. Song, J. Xiao, J. Du, P. Tao, T. Sun, M. Shao, T. Wang, Degradation of phenol by coal-based carbon membrane integrating sulfate radicals-based advanced oxidation processes, Ecotox. Environ. Safe. 185 (2019) 109662.
[50] C. Wang, H. Wang, R. Luo, C. Liu, J. Li, X. Sun, J. Shen, W. Han, L. Wang, Metal-organic framework one-dimensional fibers as efficient catalysts for activating peroxymonosulfate, Chem. Eng. J. 330 (2017) 262-271.
[51] J. Sheng, H. Yin, F. Qian, H. Huang, S. Gao, J. Wang, Reduced graphene oxide-based composite membranes for *in-situ* catalytic oxidation of sulfamethoxazole operated in membrane filtration, Sep. Purif. Technol. 236 (2020) 116275.
[52] J. Ye, C. Li, L. Wang, Y. Wang, J. Dai, Synergistic multiple active species for catalytic self-cleaning membrane degradation of persistent pollutants by activating peroxymonosulfate, J. Colloid Interface Sci. 587 (2021) 202-213.
[53] N. Li, G. Chen, J. Zhao, B. Yan, Z. Cheng, L. Meng, V. Chen, Self-cleaning PDA/ZIF-67@PP membrane for dye wastewater remediation with peroxymonosulfate and visible light activation, J. Membr. Sci. 591 (2019) 117341.
[54] Z.S. Zhu, J. Qu, S.M. Hao, S. Han, K.L. Jia, Z.Z. Yu, α-Fe_2O_3 nanodisk/bacterial cellulose hybrid membranes as high-performance sulfate-radical-based visible light photocatalysts under stirring/flowing states, ACS Appl. Mater. Interfaces 10 (2018) 30670-30679.
[55] A. Aher, J. Papp, A. Colburn, H. Wan, E. Hatakeyama, P. Prakash, B. Weaver, D.

973 Bhattacharyya, Naphthenic acids removal from high TDS produced water by persulfate
974 mediated iron oxide functionalized catalytic membrane, and by nanofiltration, Chem.
975 Eng. J. 327 (2017) 573-583.
976 [56] Y. Liu, L. Yu, C.N. Ong, J. Xie, Nitrogen-doped graphene nanosheets as reactive
977 water purification membranes, Nano Res. 9 (2016) 1983-1993.
978 [57] L.C. Zhang, Z. Jia, F. Lyu, S.X. Liang, J. Lu, A review of catalytic performance of
979 metallic glasses in wastewater treatment: recent progress and prospects, Prog. Mater.
980 Sci. 105 (2019) 100576.
981 [58] J.J. Kruzic, Bulk metallic glasses as structural materials: a review, Adv. Eng. Mater.
982 18 (2016) 1308-1331.
983 [59] F. Hu, S. Zhu, S. Chen, Y. Li, L. Ma, T. Wu, Y. Zhang, C. Wang, C. Liu, X. Yang,
984 L. Song, X. Yang, Y. Xiong, Amorphous metallic NiFeP: a conductive bulk material
985 achieving high activity for oxygen evolution reaction in both alkaline and acidic media,
986 Adv. Mater. 29 (2017) 1606570.
987 [60] S.X. Liang, X. Wang, W. Zhang, Y.J. Liu, W. Wang, L.C. Zhang, Selective laser
988 melting manufactured porous Fe-based metallic glass matrix composite with
989 remarkable catalytic activity and reusability, Appl. Mater. Today 19 (2020) 100543.
990 [61] Z. Jia, X. Duan, W. Zhang, W. Wang, H. Sun, S. Wang, L.C. Zhang, Ultra-
991 sustainable $Fe_{78}Si_9B_{13}$ metallic glass as a catalyst for activation of persulfate on
992 methylene blue degradation under UV-Vis light, Sci. Rep. 6 (2016) 38520.
993 [62] S.X. Liang, Z. Jia, W.C. Zhang, X.F. Li, W.M. Wang, H.C. Lin, L.C. Zhang,
994 Ultrafast activation efficiency of three peroxides by $Fe_{78}Si_9B_{13}$ metallic glass under
995 photo-enhanced catalytic oxidation: a comparative study, Appl. Catal. B Environ. 221
996 (2018) 108-118.
997 [63] S.X. Liang, Z. Jia, W.C. Zhang, W.M. Wang, L.C. Zhang, Rapid malachite green
998 degradation using $Fe_{73.5}Si_{13.5}B_9Cu_1Nb_3$ metallic glass for activation of persulfate under
999 UV-Vis light, Mater. Des. 119 (2017) 244-253.
1000 [64] Z. Jia, Q. Wang, L. Sun, Q. Wang, L.C. Zhang, G. Wu, J.H. Luan, Z.B. Jiao, A.
1001 Wang, S.X. Liang, M. Gu, J. Lu, Metallic glass catalysts: attractive *in situ* self-
1002 reconstructed hierarchical gradient structure of metallic glass for high efficiency and
1003 remarkable stability in catalytic performance, Adv. Funct. Mater. 29 (2019) 1970131.
1004 [65] K.J. de France, T. Hoare, E.D. Cranston, Review of hydrogels and aerogels
1005 containing nanocellulose, Chem. Mater. 29 (2017) 4609-4631.
1006 [66] C. Wan, Y. Jiao, S. Wei, L. Zhang, Y. Wu, J. Li, Functional nanocomposites from
1007 sustainable regenerated cellulose aerogels: a review, Chem. Eng. J. 359 (2019) 459-475.
1008 [67] Q. Liao, X. Su, W. Zhu, W. Hua, Z. Qian, L. Liu, J. Yao, Flexible and durable
1009 cellulose aerogels for highly effective oil/water separation, RSC Adv. 6 (2016) 63773-
1010 63781.
1011 [68] W. Ren, J. Gao, C. Lei, Y. Xie, Y. Cai, Q. Ni, J. Yao, Recyclable metal-organic

framework/cellulose aerogels for activating peroxymonosulfate to degrade organic pollutants, Chem. Eng. J. 349 (2018) 766-774.
[69] P. Hu, M. Long, X. Bai, C. Wang, C. Cai, J. Fu, B. Zhou, Y. Zhou, Monolithic cobalt-doped carbon aerogel for efficient catalytic activation of peroxymonosulfate in water, J. Hazard. Mater. 332 (2017) 195-204.
[70] X.J. Yu, J. Qu, Z. Yuan, P. Min, S.M. Hao, Z.S. Zhu, X. Li, D. Yang, Z.Z. Yu, Anisotropic $CoFe_2O_4$@Graphene hybrid aerogels with high flux and excellent stability as building blocks for rapid catalytic degradation of organic contaminants in a flow-type setup, ACS Appl. Mater. Interfaces 11 (2019) 34222-34231.
[71] Y. Hu, Z. Li, J. Yang, H. Zhu, Degradation of methylparaben using BiOI-hydrogel composites activated peroxymonosulfate under visible light irradiation, Chem. Eng. J. 360 (2019) 200-211.
[72] Y. Guo, J. Bae, Z. Fang, P. Li, F. Zhao, G. Yu, Hydrogels and hydrogel-derived materials for energy and water sustainability, Chem. Rev. 120 (2020) 7642-7707.
[73] Q. Yi, J. Tan, W. Liu, H. Lu, M. Xing, J. Zhang, Peroxymonosulfate activation by three-dimensional cobalt hydroxide/graphene oxide hydrogel for wastewater treatment through an automated process, Chem. Eng. J. 400 (2020) 125965.
[74] L. Duan, X. Zhou, S. Liu, P. Shi, W. Yao, 3D-hierarchically structured Co_3O_4/graphene hydrogel for catalytic oxidation of Orange II solutions by activation of peroxymonosulfate, J. Taiwan Inst. Chem. Eng. 76 (2017) 101-108.
[74] L. Duan, X. Zhou, S. Liu, P. Shi, W. Yao, 3D-hierarchically structured Co_3O_4/graphene hydrogel for catalytic oxidation of Orange II solutions by activation of peroxymonosulfate, J. Taiwan Inst. Chem. Eng. 76 (2017) 101-108.
[75] D. Gan, Z. Huang, X. Wang, L. Jiang, C. Wang, M. Zhu, F. Ren, L. Fang, K. Wang, C. Xie, X. Lu, Graphene oxide-templated conductive and redox-active nanosheets incorporated hydrogels for adhesive bioelectronics, Adv. Funct. Mater. 30 (2020) 1907678
[76] Z. Wang, Y. Cong, J. Fu, Stretchable and tough conductive hydrogels for flexible pressure and strain sensors, J. Mater. Chem. B 8 (2020) 3437-3459.
[77] X. Zhao, Y. Liang, Y. Huang, J. He, Y. Han, B. Guo, Physical double-network hydrogel adhesives with rapid shape adaptability, fast self-healing, antioxidant and NIR/pH stimulus-responsiveness for multidrug-resistant bacterial infection and removable wound dressing, Adv. Funct. Mater. 30 (2020) 1910748.
[78] Y. Zhuang, X. Wang, L. Zhang, D.D. Dionysiou, Z. Kou, B. Shi, Double-network hydrogel templated FeS/graphene with enhanced PMS activation performance: considering the effect of the template and iron species, Environ. Sci.: Nano 7 (2020) 817-828.
[79] C. Wang, P. Zhang, W. Xiao, J. Zhao, M. Shi, H. Wei, Z. Deng, B. Guo, Z. Zheng, Y. Yu, Visible-light-assisted multimechanism design for one-step engineering tough

hydrogels in seconds, Nat. Commun. 11 (2020) 4694.
[80] R.D.C. Soltani, M. Mahmoudi, G. Boczkaj, A. Khataee, Activation of peroxymonosulfate using carbon black nano-spheres/calcium alginate hydrogel matrix for degradation of acetaminophen: Fe_3O_4 co-immobilization and microbial community response, J. Ind. Eng. Chem. 91 (2020) 240-251.
[81] A. Hussain, Y. Liu, T. Bin-Aftab, D. Li, W. Sand, Engineering reusable sponge of cobalt heterostructures for highly efficient organic pollutants degradation via peroxymonosulfate activation, ChemNanoMat 5 (2019) 547-557.
[82] M. Sayed, J.A. Khan, L.A. Shah, N.S. Shah, F. Shah, H.M. Khan, P. Zhang, H. Arandiyan, Solar light responsive poly(vinyl alcohol)-assisted hydrothermal synthesis of immobilized TiO_2/Ti film with the addition of peroxymonosulfate for photocatalytic degradation of ciprofloxacin in aqueous media: a mechanistic approach, J. Phys. Chem. C 122 (2018) 406-421.
[83] J. Lim, Y. Yang, M.R. Hoffmann, Activation of peroxymonosulfate by oxygen vacancies-enriched cobalt-doped black TiO_2 nanotubes for the removal of organic pollutants, Environ. Sci. Technol. 53 (2019) 6972-6980.
[84] X. Wang, X. Zhang, L. Dai, H. Guo, P. Shi, Y. Min, Q. Xu, Recycling the cathode scrap of spent lithium-ion batteries as an easily recoverable peroxymonosulfate catalyst with enhanced catalytic performance, ACS Sustain. Chem. Eng. 8 (2020) 11337-11347.
[85] Y. Yao, H. Hu, H. Yin, M. Yu, H. Zheng, Y. Zhang, S. Wang, Phase change on stainless-steel mesh for promoting sulfate radical formation via peroxymonosulfate oxidation, Appl. Catal. B Environ. 278 (2020) 119333.
[86] D. Gao, M. Junaid, F. Lin, S. Zhang, N. Xu, Degradation of sulphachloropyridazine sodium in column reactor packed with $CoFe_2O_4$-loaded quartz sand via peroxymonosulfate activation: insights into the amorphous phase, efficiency, and mechanism, Chem. Eng. J. 390 (2020) 124549.
[87] X. Yang, J. Cai, X. Wang, Y. Li, Z. Wu, W.D. Wu, X.D. Chen, J. Sun, S.P. Sun, Z. Wang, A bimetallic Fe–Mn oxide-activated oxone for *in situ* chemical oxidation (ISCO) of trichloroethylene in groundwater: efficiency, sustained activity, and mechanism investigation, Environ. Sci. Technol. 54 (2020) 3714-3724.
[88] M. Yao, B. Sun, N. Wang, W. Hu, S. Komarneni, Self-generated N-doped anodized stainless steel mesh for an efficient and stable overall water splitting electrocatalyst, Appl. Surf. Sci. 480 (2019) 655-664.
[89] H. Lin, J. Wu, H. Zhang, Degradation of clofibric acid in aqueous solution by an EC/Fe^{3+}/PMS process, Chem. Eng. J. 244 (2014) 514-521.
[90] J. Wu, H. Zhang, J. Qiu, Degradation of Acid Orange 7 in aqueous solution by a novel electro/Fe^{2+}/peroxydisulfate process, J. Hazard. Mater. 215-216 (2012) 138-145.
[91] H. Zhang, Z. Wang, C. Liu, Y. Guo, N. Shan, C. Meng, L. Sun, Removal of COD from landfill leachate by an electro/Fe^{2+}/peroxydisulfate process, Chem. Eng. J. 250

(2014) 76-82.
[92] S. Yuan, P. Liao, A.N. Alshawabkeh, Electrolytic manipulation of persulfate reactivity by iron electrodes for trichloroethylene degradation in groundwater, Environ. Sci. Technol. 48 (2014) 656-663.
[93] C. Nie, Z. Ao, X. Duan, C. Wang, S. Wang, T. An, Degradation of aniline by electrochemical activation of peroxydisulfate at MWCNT cathode: the proofed concept of nonradical oxidation process, Chemosphere 206 (2018) 432-438.
[94] H. Luo, C. Li, C. Wu, W. Zheng, X. Dong, Electrochemical degradation of phenol by *in situ* electro-generated and electro-activated hydrogen peroxide using an improved gas diffusion cathode, Electrochim. Acta 186 (2015) 486-493.
[95] H. Song, L. Yan, J. Ma, J. Jiang, G. Cai, W. Zhang, Z. Zhang, J. Zhang, T. Yang, Nonradical oxidation from electrochemical activation of peroxydisulfate at Ti/Pt anode: efficiency, mechanism and influencing factors, Water Res. 116 (2017) 182-193.
[96] A. Farhat, J. Keller, S. Tait, J. Radjenovic, Removal of persistent organic contaminants by electrochemically activated sulfate, Environ. Sci. Technol. 49 (2015) 14326-14333.
[97] K.Y. Foo, B.H. Hameed, A short review of activated carbon assisted electrosorption process: an overview, current stage and future prospects, J. Hazard. Mater. 170 (2009) 552-559.
[98] C. Nie, Z. Dai, H. Meng, X. Duan, Y. Qin, Y. Zhou, Z. Ao, S. Wang, T. An, Peroxydisulfate activation by positively polarized carbocatalyst for enhanced removal of aqueous organic pollutants, Water Res. 166 (2019) 115043.
[99] Z. Liu, B. Ren, H. Ding, H. He, H. Deng, C. Zhao, P. Wang, D.D. Dionysiou, Simultaneous regeneration of cathodic activated carbon fiber and mineralization of desorbed contaminations by electro-peroxydisulfate process: advantages and limitations, Water Res. 171 (2020) 115456.
[100] Z. Liu, C. Zhao, P. Wang, H. Zheng, Y. Sun, D.D. Dionysiou, Removal of carbamazepine in water by electro-activated carbon fiber-peroxydisulfate: comparison, optimization, recycle, and mechanism study, Chem. Eng. J. 343 (2018) 28-36.
[101] H. Ding, Y. Zhu, Y. Wu, J. Zhang, H. Deng, H. Zheng, Z. Liu, C. Zhao, *In situ* regeneration of phenol-saturated activated carbon fiber by an electro-peroxymonosulfate process, Environ. Sci. Technol. 54 (2020) 10944-10953.
[102] Y. Zhang, W. Kang, H. Yu, S. Chen, X. Quan, Electrochemical activation of peroxymonosulfate in cathodic micro-channels for effective degradation of organic pollutants in wastewater, J. Hazard. Mater. 398 (2020) 122879.
[103] S. Han, S.U. Hassan, Y. Zhu, S. Zhang, H. Liu, S. Zhang, J. Li, Z. Wang, C. Zhao, Significance of activated carbon fiber as cathode in electro/Fe^{3+}/peroxydisulfate oxidation process for removing carbamazepine in aqueous environment, Ind. Eng. Chem. Res. 58 (2019) 19709-19718.

[104] M. Zhang, Y. Gong, N. Ma, X. Zhao, Promoted photoelectrocatalytic degradation of BPA with peroxymonosulfate on a $MnFe_2O_4$ modified carbon paper cathode, Chem. Eng. J. 399 (2020) 125088.
[105] K. Wang, G. Liang, M. Waqas, B. Yang, K. Xiao, C. Zhu, J. Zhang, Peroxymonosulfate enhanced photoelectrocatalytic degradation of ofloxacin using an easily coated cathode, Sep. Purif. Technol. 236 (2020) 116301.
[106] J. Liu, G. Han, D. Zhao, K. Lu, J. Gao, T.S. Chung, Self-standing and flexible covalent organic framework (COF) membranes for molecular separation, Sci. Adv. 6 (2020) eabb1110.
[107] Y. Liu, R. Guo, G. Shen, Y. Li, Y. Li, J. Gou, X. Cheng, Construction of CuO@CuS/PVDF composite membrane and its superiority for degradation of antibiotics by activation of persulfate, Chem. Eng. J. 405 (2021) 126990.
[108] Z. Wang, L.C. Nengzi, X. Zhang, Z. Zhao, X. Cheng, Novel $NiCo_2S_4$/CS membranes as efficient catalysts for activating persulfate and its high activity for degradation of nimesulide, Chem. Eng. J. 381 (2020) 122517.
[109] C. Chen, M. Xie, L. Kong, W. Lu, Z. Feng, J. Zhan, Mn_3O_4 nanodots loaded g-C_3N_4 nanosheets for catalytic membrane degradation of organic contaminants, J. Hazard. Mater. 390 (2020) 122146.
[110] J. Kang, H. Zhang, X. Duan, H. Sun, X. Tan, S. Liu, S. Wang, Magnetic Ni-Co alloy encapsulated N-doped carbon nanotubes for catalytic membrane degradation of emerging contaminants, Chem. Eng. J. 362 (2019) 251-261.
[111] A. Aher, S. Thompson, T. Nickerson, L. Ormsbee, D. Bhattacharyya, Reduced graphene oxide-metal nanoparticle composite membranes for environmental separation and chloro-organic remediation, RSC Adv. 9 (2019) 38547-38557.
[112] K. Govindan, M. Raja, M. Noel, E.J. James, Degradation of pentachlorophenol by hydroxyl radicals and sulfate radicals using electrochemical activation of peroxomonosulfate, peroxodisulfate and hydrogen peroxide, J. Hazard. Mater. 272 (2014) 42-51.
[113] Y.R. Wang, W. Chu, Degradation of 2, 4, 5-trichlorophenoxyacetic acid by a novel Electro-Fe(II)/Oxone process using iron sheet as the sacrificial anode, Water Res. 45 (2011) 3883-3889.

Figure captions

Fig. 1. Heterogeneous activation mechanism of persulfates, and challenges to nanocatalysts in persulfate-based-AOPs

Fig. 2. Construction strategy for persulfate activation systems based on immobilized nanocatalysts

Fig. 3. Typical composite membrane prepared via ceramic and polymeric substances, and then used in immersion mode reaction systems: (a) synthetic procedure for PAN-Co ceramic membrane, with SEM surface images of (a-1) initial Al_2O_3 membrane, and (a-2) functionalized PAN-Co-C membrane, and SEM cross-section images of (a-3) initial Al_2O_3 membrane, and (a-4) functionalized PAN-Co-C membrane (reprinted with permission from [26], copyright 2019 Elsevier); (b) synthetic procedure for LDH@PVDF membrane (reprinted with permission from [27], copyright 2020 Elsevier); and (c) synthetic procedure for NSC-Fe@PVDF membranes, with (c-1) digital photograph of NSC-Fe@PVDF membrane and (c-2) color changes of Orange II in NSC-Fe@PVDF/PMS system (reprinted with permission from [28], copyright 2017 Elsevier).

Fig. 4. Typical composite membrane prepared from nanofibers through filtration, and used in immersion mode reaction systems: (a) synthetic procedure, (b) SEM image of Co/Fe bi- MOFs/CNFs membrane (reprinted with permission from [32], copyright 2020 Elsevier); and (c) schematic representation of magnetic nanocellulose membrane preparation and PMS activation process (reprinted with permission from [33], copyright 2020 Elsevier).

Fig. 5. Typical composite membrane prepared from electrospun nanofibers, and used in immersion mode reaction systems: (a) synthetic procedure for metallic Cu-doped C/SiO_2

nanofibers (CINMs) by sol-gel electrospinning method; (b) SEM image of α-Fe@carbon ENFs (reprinted with permission from [38], Copyright 2017 RSC); (c) SEM image of CINMs; and (d) optical photograph showing that the CINMs could be folded into a paper crane without any fracturing (reprinted with permission from [39], copyright 2019 RSC).

Fig. 6. Schematic illustration of reaction mechanism for organic removal by (a) Co/Fe bi-MOFs/cellulose NFs membrane/PMS system (reprinted with permission from [32], copyright 2020 Elsevier), and (b) NSC-Fe@PVDF/PMS system (reprinted with permission from [28], copyright 2017 Elsevier).

Fig. 7. Typical composite membranes used in filtration mode reaction systems based on vacuum filtration: (a) synthetic procedure, SEM images, and water treatment method for ZIF-67/PAN membrane (reprinted with permission from [50], copyright 2017 Elsevier); (b) synthetic procedure, SEM images, digital photos and water treatment method for CoCu LDH-CGF membrane and pristine CGF membrane. (reprinted with permission from [27], copyright 2020 Elsevier); and (c) schematic diagram of the experimental setup under recirculation mode (configuration A) and continuous mode (configuration B). (reprinted with permission from [23, 47], copyright 2019 and 2020 Elsevier); the digital photograph depicts elements in the filtration reaction system with recirculation and continuous modes (reprinted with permission from [51], copyright 2020 Elsevier).

Fig. 8. Typical composite membrane used in filtration mode reaction systems based on cross-flow filtration: (a) top-section SEM images of pristine PVDF membrane and CoFe-NMTs-800/PVDF membrane, cross-section SEM image of CoFe-NMTs-800/PVDF membrane, and metal leaching concentration after five runs in CoFe-NMTs-800/PMS system (reprinted with permission from [52], copyright 2021 Elsevier); (b) schematic representation of integration of nanofiltration membranes and Fe_xO_y functionalized

membranes for treatment of naphthenic acid from produced water (reprinted with permission from [55], copyright 2017 Elsevier); (c) schematic depiction of the Flowing Bed Device (reprinted with permission from [54], copyright 2018 ACS); and (d) cross-flow filtration apparatus with light irradiation (reprinted with permission from [53], copyright 2019 Elsevier).

Fig. 9. Typical metallic glasses used in persulfate-AOPs: (a) schematic diagram of melt-spinning process for manufacturing glassy ribbons and an optical photograph of typical product (reprinted with permission from [57], copyright 2019 Elsevier); (b) comparison of the catalytic stability of different iron-based materials (reprinted with permission from [64], copyright 2019 Wiley); and (c) synthetic procedure, SEM images, and reusability of as-produced Fe-based MG matrix composite (Fe-based MG_{PDS-45}: the Fe-based MG_{PDS-45} after 45-times use in PDS activation process; Fe-based $MG_{Fenton-45}$: the Fe-based MG_{PDS-45} after 45-times use in Fenton-like reaction process) (reprinted with permission from [60], copyright 2020 Elsevier).

Fig. 10. Typical aerogels and hydrogels used in persulfate-AOPs: (a) photographs of ZIF-based hybrid aerogels (reprinted with permission from [68], copyright 2018 Elsevier); (b) elimination of phenol under different conditions, and photographs of CoCA in water (inset) (reprinted with permission from [69], copyright 2020 Elsevier); (c) schematic illustration of the preparation of an anisotropic $CoFe_2O_4$@GA-A and its application for the continuing treatment of wastewater with a flow-type setup (reprinted with permission from [70], copyright 2020 Elsevier); (d) plots of removal efficiencies of organic pollutants for $CoFe_2O_4$@GA-A and $CoFe_2O_4$@GA-I at different flow rates, and a photograph of real-time catalytic experiments using $CoFe_2O_4$@GA-A and stacked $CoFe_2O_4$@GA-As (each red arrow indicates a piece of $CoFe_2O_4$@GA-A) (reprinted with permission from

[70], copyright 2019 ACS); (e) schematic illustration of degradation equipment flowchart based on CoOOH/GO hydrogel composite (reprinted with permission from [73], copyright 2019 ACS); and (f) preparation routine and photographs of samples (reprinted with permission from [78], copyright 2020 RSC).

Fig. 11. Specific materials based on uncommon supports prepared for persulfate activation: (a) digital images of as-obtained SP-50 sponge cut into different geometrical shapes; SEM images of (1) SP-50 sponge and (2) SP-50; digital photograph of SP-50/PMS reactive process (reprinted with permission from [81], copyright 2019 Wiley); (b) digital photograph of Co-Black TNT/PMS reactive process and the activation mechanisms (reprinted with permission from [83], copyright 2019 ACS); (c) SEM images and activation mechanisms of the stainless-steel/PMS system for degrading organic contaminants (reprinted with permission from [85], copyright 2020 Elsevier); (d) recycling process of spent lithium-ion battery (reprinted with permission from [84], copyright 2020 ACS); and (e) schematic illustration of PMS-based *in situ* chemical oxidation process and the sand columns (5 cm internal diameter × 50 cm length) working mode (reprinted with permission from [87], copyright 2020 ACS).

Fig. 12. Electrocatalytic auxiliary systems constructed for persulfate activation: (a) schematic diagram of electrochemical activation of PDS and aniline degradation experiment (reprinted with permission from [93], Copyright 2018 Elsevier); (b) proposed mechanism of organic pollutant removal by asymmetric quasi capacitive deionization (AQCDI)/PDS/1.2V system (R represents the organic molecule and X represents the active sites in MWCNTs) (reprinted with permission from [98], copyright 2019 Elsevier); (c) SEM images of the ACF in different reaction systems (reprinted with permission from [99, 100], copyright 2018 and 2020 Elsevier); (d) schematic representation of ACF

Regeneration experimental setup (reprinted with permission from [101], copyright 2020 ACS); and (e) schematic diagram of the E-PMS activation mechanism via FTC and FBC strategy (reprinted with permission from [102], copyright 2020 ACS).

Table 1. Summary of recent studies on catalytic membranes for persulfate activation in batch mode

Catalytic component and support material	Experimental conditions	Pollutant removal	Metal leaching (mg/L)	Fabrication method	Regeneration method	Reaction mode
Co embedded carbon (dip-coating) Al_2O_3 (20 nm pore size) [26]	Membrane weight: 100 mg Transmembrane pressure: 1 bar $[Sulfamethoxazole]_0$=10 mg/L $[PMS]_0$=0.1 g/L *T*=room temperature $pH_{solution}$=not reported *t*=60 min	Over 90%	[Co]=0.05	Dip-coating and carbonization method	Not studied	**Batch mode** Immersion
NSC-Fe PVDF [28]	$[Orange\ II]_0$=20 mg/L *V*=250 mL $[PDS]_0$=0.6 g/L *T*=25 °C $pH_{solution}$ (unadjusted) *t*=150 min Single piece of membrane (24 cm^2)	98% (in 1st cycle) ~78% (in 4th cycle)	[Fe]=0.037	Phase inversion technique	Filtered and washed with ultrapure water after each cycle	**Batch mode** Magnetic stirring
CoCu LDH PVDF [27]	$[Sulfamethoxazole]_0$=10 mg/L *V*=100 mL $[PMS]_0$=150 mg/L *T*=25 °C $pH_{solution}$=5.77 (unadjusted) *t*=60 min Single piece of membrane (5×10 cm^2) (catalyst	Over 90% (from 1st cycle to 10th cycle)	[Co]=0.044, [Cu]=0.026 (nanocatalysts [Co]=0.157, [Cu]=0.174)	Phase inversion technique	Washed with deionized water and ethanol after each cycle	**Batch mode** Magnetic stirring

	7.00 wt.%)					
CuO@CuS PVDF [107]	$[Organics]_0$=10 mg/L *V*=100 mL $[PDS]_0$=0.4 g/L *T*=25 °C $pH_{solution}$=7.34 (unadjusted) *t*=60 min Single piece of membrane (5×5 cm^2) (catalyst 20.00 wt.%)	83.4% (Tetracycline), about 50% (Enrofloxacin), about 45% (Ciprofloxacin), 40.8% (Lomefloxacin)	[Cu]=1.664 (nanocatalysts [Cu]=2.147)	Phase inversion technique	Washed with ethanol after each cycle	**Batch mode** Magnetic stirring
Co/Fe bi-MOFs CNFs as fiber support and unspecified organic substrate (0.22 μm pore size) as membrane support [32]	Single piece of membrane with 20 mg catalyst *V*=100 mL $[Tetrabromobisphenol\ A]_0$=50 mg/L $[PMS]_0$=0.1 mM *T*=room temperature $pH_{solution}$=7.5 *t*=30 min	100% (in 1st cycle) 60% (in 5th cycle)	Not reported	Vacuum filtration	Rinsed and freeze-dried	**Batch mode** Immersion
Fe_3O_4 CNFs [33]	*V*=100 mL $[Rhodamine\ B]_0$=20 mg/L $[PMS]_0$=1.0 g/L *T* and $pH_{solution}$ not reported *t*=300 min	Not reported	Not reported	*In situ* co-precipitation method and filtration	Not studied	**Batch mode** Magnetic stirring
α-Fe@carbon composite NFs [38]	Membrane weight=10 mg $[Methyl\ blue]_0$=10 mg/L *V*=100 mL	100% (in 1st cycle) 90% (in 5th cycle)	Not reported	Electrospinning method and carbonization in an	Not illustrated	**Batch mode** Magnetic stirring

	[PMS]$_0$=0.5 g/L *T*=25 °C pH$_{solution}$ (unadjusted) *t*=15 min			N_2 atmosphere environment		
Metallic Cu-doped C/SiO_2 nanofibers (CINMs) [39]	Membrane weight=0.3 g/L [Tetracycline]$_0$=50 mg/L *V*=10 mL [PDS]$_0$=0.3 g/L *T*=55 °C pH$_{solution}$=9 (adjusted) *t*=40 min	95% (in 1st cycle) Over 90% (in 5th cycle)	[Cu]=0.18 (pH=7, after 10 min) [Cu]=0.37 ((pH=7, after 40 min)	Electrospinning method and carbonization in an N_2 atmosphere environment	Washed with deionized water and ethanol, dried in an air-circulating	**Batch mode** Magnetic stirring
Co–Al_2O_3 NFs membrane [41]	Membrane weight=10 mg (catalyst 11.00 wt.%) [Bisphenol A]$_0$=20 mg/L *V*=10 mL [PMS]$_0$=1 mM *T*=25 °C pH$_{solution}$=7 (buffered) *t*=40 min	100%	[Co]=0.10 ± 0.4 [Al]=0.09 ± 0.09	Electrospinning method	Not studied	**Batch mode** Mechanical stirring
Pt-Al_2O_3 NFs membrane [42]	Membrane weight=1.0 g/L (catalyst 6 wt.%) *V*=10 mL [Bisphenol A]$_0$=20 mg/L [PMS]$_0$=2 mM *T*=room temperature pH$_{solution}$=7.0 (buffered) *t*=20 min	100% 97% and 88% (in the 1st, 2nd and 3rd cycle, respectively) 100% (stored for one week) 97% (stored for one month)	No Pt leaching [Al]=0.37	Electrospinning method	Not illustrated	**Batch mode** Rotary shake

		87% (stored for one year)				
	Membrane weight=1.0 g/L (catalyst 6 wt.%) V=10 mL [Bisphenol A]$_0$=20 mg/L [PMS]$_0$=2 mM T=room temperature pH$_{solution}$=7.0 (buffered) t=20 min	100%	Not reported	Electrospinning method	Not illustrated	**Batch mode** Mechanical stirring
Ag-LCF Initial spinning mixture composed of Ag-LCF powder, polyethersulfone (PESF), and 1-methyl-2-pyrrolidinone (NMP) [43]	Membrane 30 cm long (catalyst 61.5 wt.%) [Methyl blue]$_0$=10 ppm Q=26 mL/min [PMS]$_0$=0.6 mM T, t, and pH$_{solution}$ not reported	Over 90% (in the 1st to 4th cycles) Less than 70% (in 5th cycle)	Not reported	Combined phase inversion and sintering method	Not illustrated	**Batch mode** Surface flow

Table 2. Summary of recent studies on catalytic membranes for persulfate activation in a filtration system

Catalytic component and support material	Experimental conditions	Pollutant removal	Metal leaching (mg/L)	Fabrication method	Regeneration method	Filtration mode
ZIF-67 PAN (Mw = 150,000) [46]	Membrane weight=40 mg (catalyst 50 wt.%) $[Acid\ yellow\text{-}17]_0$=500 mg/L *V*=200 mL $[PMS]_0$=0.5 g/L *T*=25 °C $pH_{solution}$ (unadjusted) *t*=10 min	95.1% (in 1st cycle) 93.9% (in 5th cycle)	Not reported	In situ electrospinning method	Not illustrated	**Batch mode** Magnetic stirring
CoCu LDH CGF as fiber support and PES as membrane support [27]	About 60 s with −0.8 MPa *V*=100 mL $[Sulfamethoxazole]_0$=10 mg/L $[PMS]_0$=500 mg/L, $pH_{solution}$=5.77 (unadjusted) *T*=25 °C Single piece of membrane (12 cm^2)	92.9% (about 60 s) 92.3% (about 60 s, in 10th cycle)	[Co]=1.605, [Cu]=1.919 (nanocatalysts [Co]=0.157, [Cu]=0.174)	Vacuum filtration	Washed with deionized water and ethanol after each cycle	**Batch filtrating mode** Pressure filtration
CoCu LDH PAN as fiber support and PES as membrane support [30]	About 60 s with −0.8 MPa *V*=100 mL $[Sulfamethoxazole]_0$=10 mg/L $[PMS]_0$=0.65 mM $pH_{solution}$=5.77 (unadjusted) *T*=25 °C Single piece of membrane (12 cm^2)	95.81% (about 60 s) 94.66% (about 60 s, in 8th cycle) 94.96% (about 60 s, in 10th cycle)	[Co]=0.037, [Cu]=0.023 (nanocatalysts [Co]=0.157, [Cu]=0.174)	Vacuum filtration	Washed with deionized water and ethanol after each cycle	**Batch filtrating mode** Pressure filtration

Ni-Co embedded carbon spheres Unspecified organic substrate (0.22 μm pore size) as membrane support [108]	[Nimesulide]$_0$=5 mg/L V=50 mL [PDS]$_0$=0.4 g/L T=25 °C pH$_{solution}$=7 t=10 min	94% (after 10 min) 81% (6th cycle)	[Ni]=0.05 [Co]=0.15	Vacuum filtration	Washed with deionized water and ethanol after each cycle	**Batch filtrating mode** Pressure filtration
Mn_3O_4 embedded g-C_3N_4 PTFE (0.22 mm pore size) as membrane support [109]	[4-Chlorophenol]$_0$=12.9 mg/L V=20 mL [PMS]$_0$=0.15 g/L T=25 °C pH$_{solution}$ not reported t=60 min	90% (after 60 min) 80% (5th cycle)	[Mn]=9.9	Vacuum filtration	Washed with deionized water and ethanol after each cycle	**Batch filtrating mode** Pressure filtration
Ni-Co encapsulated N-doped CNTs PTFE (0.45 mm pore size) as membrane support [110]	[Ibuprofen]$_0$=500 μg/L V=200 mL [PMS]$_0$=0.1 g/L T=25 °C pH$_{solution}$=7.2 (buffered) t=20 min (each recirculation)	~70% (after 20 min) 100% (after 80 min) ~70% (after 80 min, in 4th cycle)	[Ni]=0.13 [Co]=0.18 (after 80 min)	Vacuum filtration	Washed with deionized water after each cycle; after the third cycle, the used catalyst was heated in argon at 350 °Cfor 3 h.	**Semi-continuous mode (under recirculation)** Under gravity
N-doped rGO PTFE (0.45 mm pore size) as	[Phenol]$_0$=5 mg/L or [Oxalic acid]$_0$=30 mg/L Q=1.5 mL/min	Phenol 30% (after 6.5 h)	Metal free	Vacuum filtration	Without regeneration	**Continuous mode**

membrane support [47]	$[PDS]_0$=238 mg/L *T*=25 °C $pH_{solution}$=inherent pH (~7.0 for phenol; 3.0 for oxalic acid) *t*=6.5 h	Oxalic acid 65% (after 6.5 h)			treatment	Pressure filtration
rGO/CNTs nylon substrate as membrane support [51]	$[Sulfamethoxazole]_0$=500 μg/L *Q*=1.0 mL/min $[PDS]_0$=1190 mg/L *T*=25 °C $pH_{solution}$ not reported *t*=3 h	77% (after 3 h)	Metal free	Vacuum filtration	Without regeneration treatment	**Continuous mode** Pressure filtration
N-doped rGO PTFE (0.45 mm pore size) as membrane support [56]	$[Phenol]_0$=47 mg/L *Q*=1.5 mL/min $[PDS]_0$=238 m/L *T*=25 °C $pH_{solution}$=6.5 *t*=3 h	~80% (after 3 h)	Metal free	Vacuum filtration	Washed with deionized water	**Continuous mode** Pressure filtration
rGO–ion nanoparticle PVDF membrane support [111]	$[Trichloroethylene]_0$=0.2 mM Transmembrane pressure=0.4 bar $[PDS]_0$=2 mM *T*=23 °C $pH_{solution=}$7 *t*=3 h	~85(over 17h)	Iron leaching was around 8%	Vacuum filtration	Without regeneration treatment	**Continuous mode** Pressure filtration

Co-TPML PVDF membrane support [45]	[Bisphenol A]$_0$=0.2μM Transmembrane pressure=0.5 bar [PMS]$_0$=10 mM *T*=20 °C pH$_{solution}$=3.5 (unadjusted) *t*=1 h	＞90%	[Co]<0.1 μg/L	Vacuum filtration	Not illustrated	**Continuous mode** Pressure filtration
CoFe alloy and $CoFe_2O_4$ nanoparticles encapsulated in N-doped microtube composites (CoFe-NMTs) PVDF as membrane substrate [52]	*V*=100 mL [Tetracycline, Bisphenol A or Phenol]$_0$=30 mg/L or [Orange G]$_0$=50 mg/L [PMS]$_0$=0.3 g/L pH$_{solution}$ not reported *T*=30 °C [catalyst]$_0$=0.1 g/L	Tetracycline 99.2% (70 min), Bisphenol A 98.7% (60 min), Phenol 99.5 (70 min) and Orange G 100% (50 min) Tetracycline over 95% (60 min, in 5th cycle)	[Co]=0.015, [Fe]=0.004	Phase invasion technique	Washed with deionized water and ethanol and then dried in a vacuum after each cycle	**Batch filtrating mode** Pressure filtration
ZIF-67 PP membrane support [53]	Membrane weight no reported (catalyst 31.8 wt.%) Filtration pressure=0.1 MPa Light source: Xenon lamp (300 W) [Methyl blue or Methyl orange]$_0$=20 mg/L *V*=300 mL [PMS]$_0$=0.3 mM *T*, *t* and pH$_{solution}$ not reported	TOC removal efficiency of 82.2% (Methyl blue) and 83.5% (Methyl orange) (in 1st cycle) 73.3% (Methyl blue) and 82.0% (Methyl orange) (in 1st cycle)	Not reported	*In situ* self-assembly approach	Without regeneration treatment	**Semi-continuous mode (under recirculation)** Pressure filtration
α-Fe_2O_3	Membrane, 3.8×1.6 cm^2, with catalyst of ~7.5	100% (*Q*=3 mL/h, after	Not reported	Vacuum filtration	Without	**Continuous**

bacterial cellulose [54]	mg Q=3, 6, 9 mL/h [Rhodamine B]$_0$=10 mg/L each [PMS]$_0$=0.4 g/L Light source: Xenon lamp with a 400 nm cutoff filter T, t and $pH_{solution}$ not reported	84 h) 93% (Q=6 mL/h, after 62 h) More than 87% (Q=9 mL/h, after 42 h)			regeneration treatment	**flowing bed state**
Fe_xO_y PVDF as membrane substrate [55]	Time: 24 h (for 8 h in a cycle) V=50 mL [Naphthenic acids]$_0$=48 mg/L [PDS]$_0$=17 mM $pH_{solution}$=5 T=23 °C Single piece of membrane (13.2 cm^2, Iron loading: 12 g/m^2)	50% (in 1st cycle) 15% (in 2nd cycle)	Iron leaching was around 14.4%, 12.3%, and 16.2% in three cycles, respectively.	*In situ* polymerization, ion exchange, reduction, and controlled oxidation	Not illustrated	**Batch mode** Surface flow
	Average flux=2 LMH [Naphthenic acids]$_0$=48 mg/L [PDS]$_0$=5000 mg/L (added in every cycle) $pH_{solution}$=5 T=23 °C Single piece of membrane (13.2 cm^2, Iron loading: 12 g/m^2)	44% (in 1st pass) 42% (in 2nd pass)	Not reported	*In situ* polymerization, ion exchange, reduction, and controlled oxidation	Not illustrated	**Continuous mode** Pressure filtration
rGO-N PVDF as membrane substrate	Membrane weight=23 mg (catalyst 6.4 wt.%) Q=0.1 mL min^{-1}	54% (Ofloxacin), 77% (Ciprofloxacin) and	[Mn]=9.9	Knife cast technique	Without regeneration	**Continuous mode**

[23]	[Ofloxacin, Ciprofloxacin and Enrofloxacin, simultaneously]$_0$=100 μg/L each [PDS]$_0$=25 mg/L *T*=room temperature pH$_{solution}$=inherent pH (5.9) *t*=24 h	91% (Enrofloxacin) (after 24 h)		treatment	Pressure filtration

Table 3. Recent studies on hydrogels and aerogels in persulfate-AOPs system

Catalytic component and support material	Experimental conditions	Catalytic Performance and Stability	Regeneration method	Metal leaching (mg/L)
ZIF-9 Cellulose aerogels [68]	$[P\text{-nitrophenol}]_0$=20 mg/L $[PMS]_0$=600 mg/L $[ZIF\text{-}9@GEL]_0$=600 mg/L $pH_{solution}$=6 (adjusted) *t*=130 min *T*=25 °C	About 90% (from 1st to 3rd cycle)	Washed with deionized water	[Co]=0.60 (the 1st cycle) [Co]=0.50 (the 2nd cycle) [Co]=0.30 (the 3rd cycle)
ZIF-12 Cellulose aerogels [68]	$[P\text{-nitrophenol}]_0$=20 mg/L $[PMS]_0$=600 mg/L $[ZIF\text{-}12@GEL]_0$=600 mg/L $pH_{solution}$=6 (adjusted) *t*=130 min *T*=25 °C	About 85% (from 1st to 3rd cycle)	Washed with deionized water	[Co]=0.75 (the 1st cycle) [Co]=0.60 (the 2nd cycle) [Co]=0.45 (the 3rd cycle)
Cobalt and Co_3O_4 Carbon aerogels [69]	$[Phenol]_0$=20 mg/L $[PMS]_0$=2.6 mM $[Composite]_0$=1.0 g/L $pH_{solution}$=7.5 (adjusted and buffered) *t*=60 min *T*=25 °C	87% (in 1st cycle) 84% (in 2nd cycle) 67% (in 3rd cycle)	Without regeneration treatment	[Co]=0.014 (the 1st cycle) [Co]=0.011 (the 2nd cycle) [Co]=0.004 (the 3rd cycle)

$CoFe_2O_4$ Anisotropic graphene Hybrid Aerogels [70]	[Indigo carmine]$_0$=50 ppm [PMS]$_0$=0.2 g/L [CFO@GA-A]$_0$=165.1 mm^2×11.4 mm $pH_{solution}$ unadjusted *T* not reported	100% (30 h, 60 mL/h) 91% (25 h, 90 mL/h) 85% (21 h, 120 mL/h)	Without regeneration treatment	Not reported
$CoFe_2O_4$ Isotropic graphene Hybrid Aerogels [70]	[Indigo carmine]$_0$=50 ppm [PMS]$_0$=0.2 g/L [CFO@GA-I]$_0$=165.1 mm^2×11.4 mm $pH_{solution}$ unadjusted *T* not reported	100% (4 h, 60 mL/h) and 41% (subsequent 10 h, 60 mL/h) Drop to 35% (within 5 h, 120 mL/h)	Without regeneration treatment	Not reported
BiOI p(HEA-APTM) hydrogel [71]	[Methylparaben]$_0$=50 mg/L [PMS]$_0$=30 mM [Composite]$_0$=2.0 g/L Xenon lamp (500 W) $pH_{solution}$ and *T* not reported	99% (90 min, with light irradiation) More than 80% (180 min, in dark)	Without regeneration treatment	Not reported

CoOOH/GO PAA hydrogel [73]	[Rhodamine B]$_0$=20 mg/L V=1 L [PMS]$_0$=0.15 mM 200 mg $Co(NO_3)_2 \cdot 6H_2O$ was used for CoOOH preparation $pH_{solution}$=6.0 (unadjusted) Flow rate=200 mL/min t=5 min T not reported	About 85% (in 1st cycle) Above 60% (in 10th cycle)	Calcination treatment	In **Fig. 10(e)**
Co_3O_4 Graphene hydrogel [74]	[Orange II]$_0$=0.2 mM [PMS]$_0$=1 mM [Composite]$_0$=0.05 g/L Neutral $pH_{solution}$ (buffered) t=90 min T not reported	100% (from 1st to 5th cycle)	Dried in a vacuum oven overnight without any treatment	[Co]=0.360
Carbon black nano-spheres (CBNS)/Fe_3O_4 Calcium alginate hydrogel matrix [80]	[Acetaminophen]$_0$=0.1 mM [PMS]$_0$=1.0 mM [Composite]$_0$=0.3 g/L $pH_{solution}$=5.5 (unadjusted) t=60 min T not reported	76.8% (in 1st cycle) 66.8% (in 5th cycle)	Not illustrated	No metal

FeS Graphene hydrogel [78]	[Tetracycline]$_0$=100 mg/L [PMS]$_0$=2 mM [Composite]$_0$=1.0 M $pH_{solution}$=6 (unadjusted) *t*=120 min *T*=25 ℃	92.2% (in 1st cycle) 88.3% (in 5th cycle)	Shaken in distilled water for 6 h	Not reported

Table 4. Recent studies on persulfate-AOPs with unusual materials as activators

Catalytic component and support material	Experimental conditions	Catalytic Performance and Stability	Regeneration method	Metal leaching (mg L^{-1})
Co_3O_4 Polymer sponge [81]	$[Acid\ Orange\ 7]_0$=0.3 mM $[PMS]_0$=3 mM $[Composite]_0$=0.6 g/L $pH_{solution}$=7 (adjusted and buffered) *T*=25 °C	100% (15 min, in 4th cycle) 100% (21 min, in 6th cycle) 100% (24 min, in 8th cycle)	Washed with distilled water and ethanol and dried in a vacuum after each cycle	[Co]=0.0118–0.066 (over eight runs)
TiO_2 Ti plate [82]	$[Ciprofloxacin]_0$=10 mg/L $[PMS]_0$=0.5 mM Xenon lamp (300 W) $pH_{solution}$=6.3 (No description) *t*=90 min *T* not reported	99.16% (from 1st to 5th cycle) 92% (in 6th cycle)	Dried	Not reported
Co-Black TNT Ti plate [83]	$[4\text{-chlorophenol}]_0$=100 μM $[PMS]_0$=1 mM $pH_{solution}$=7.0 (buffered) *t*=30 min *T* not reported	100% (from 1st to 15th cycle)	Without regeneration treatment	[Co]=0
Recycled active $LiMn_2O_4$ Al foil in spent lithium-ion batteries [84]	$[Ortho\text{-}phenylphenol]_0$=20 mg/L $[PMS]_0$=0.3 g/L $pH_{solution}$ not reported *t*=60 min *T* =25 °C	100% (in 1st cycle) 94.8% (in 10th cycle)	Washed with deionized water	Not reported

Surface-etched and N_2-annealed stainless-steel mesh Stainless-steel mesh [85]	[Orange II]$_0$=10 mg/L [PMS]$_0$=0.25 g/L $pH_{solution}$ unadjusted *t*=40 min *T*=25 °C	100% (from 1st to 3rd cycle)	Washed with ethanol after each cycle.	Not reported
$CoFe_2O_4$ Quartz sand [86]	*V*=1 L [Sulphachloropyridazine sodium]$_0$=20 mg/L [PMS]$_0$=75 mg/L [Composite]$_0$=0 g (1.0% $CoFe_2O_4$ loading) $pH_{solution}$=6.8 (adjusted) Flow rate=6 mL/min *T* not reported	Fresh composite: Over 80% (from 0 to 360 min) Over 75% (from 360 to 480 min) Regenerated composite: Over 80% (from 0 to 120 min)	Calcined in the muffle furnace at 300 °Cfor 4 h.	Contrary to the batch reactor, the continuous flow reactor exhibited about a quarter lower cobalt leaching.
$Mn_{1.5}FeO_{6.35}$ Sand [87]	[Trichloroethylene]$_0$=20 mg/L [PDS]$_0$=8 mM Column reactor (porosity of 25.7%) packed with sand (99.5 wt.%) and the BFMO catalysts (0.5 wt.%) $pH_{solution}$=7.0 Flow rate=1.47 L/d *T* not reported	BFMO remained stable in the sand column throughout 115-day continuous flow test period.	Not reported	Not reported

Table 5. Recent studies on electro-assistance persulfate-AOPs

Anode	Cathode	Ref.	Experimental conditions	Catalytic performance and stability
Fe sheet (4.2 cm×3 cm×0.5 cm, 25.2 cm^2)	**Fe sheet** (4.2 cm×3 cm×0.5 cm, 25.2 cm^2)	[112]	$[Pentachlorophenol]_0$=0.10 mM $[PMS]_0=9.9\times10^{-5}$ M [NaCl]=1.7 mM *t*=10 min $pH_{solution}$=4.5 (unadjusted) Current density=90 mA *T* not reported	75% (Mineralization efficiency)
			$[Pentachlorophenol]_0$=0.10 mM $[PDS]_0=9.9\times10^{-5}$ M [NaCl]=1.7 mM *t*=20 min $pH_{solution}$=6.5 (unadjusted) Current density=90 mA *T* not reported	About 60% (mineralization efficiency)
Fe sheet (10 cm^2)	**Graphite bar**	[113]	[2,4,5-Trichlorophenoxyacetic acid]$_0$=0.10 mM $[PMS]_0$=0.25 mM $[Na_2SO_4]$=50 mM *t*=30 min $pH_{solution}$ not reported (unadjusted) Current=10 mA *T*=23 ± 2 ℃	About 100%
Fe sheet (Cast gray iron, 76 mm×9.5 mm×3.2 mm)	**Mixed metal oxide sheet** (85 mm×15 mm×1.8 mm, IrO_2/Ta_2O_5 coating on titanium mesh type)	[92]	$[Trichloroethylene]_0$=0.4 mM $[PDS]_0$=5 mM *t*=20 min $pH_{solution}$=5.6 (unadjusted) Current=+100 mA *T* not reported	More than 99%
Graphite sheet (4.5 cm×4.5 cm)	**MWCNTs coating graphite sheet cathode** (with active	[93]	$[Aniline]_0$=0.45 mM $[PDS]_0$=5.55 mM *t*=150 min $pH_{solution}$ not reported	98% (in the 1st cycle) 89% (in the 9th cycle)

	materials of ~ 85 mg, 4.5 cm×4.5 cm)		Working voltage=–0.6 V *T* not reported	
Graphite sheet (4.5 cm×4.5 cm)	**MWCNTs coating graphite sheet cathode** (with active materials of ~ 10 mg, 4.5 cm×□4.5 cm)	[98]	[Acyclovir]$_0$=0.45 mM [PDS]$_0$=11.1 mM *t*=120 min (positive polarization) *t*=180 min (negative polarization) pH$_{solution}$ not reported Working voltage=1.2 V *T* not reported	Above 95% (from 1st to 3rd cycle, negative polarization) Above 95% (from 1st to 11th cycle, negative polarization)
Ti/Pt (50 mm×35 mm×1 mm)	**ACF coating Titanium plate cathode** (50 mm×35 mm×1 mm)	[103]	[Carbamazepine]$_0$=0.04 mM [PDS]$_0$=2 mM [Fe^{3+}]=0.4 mM [Na_2SO_4]=50 mM *t*=30 min pH$_{solution}$=3 (adjusted) Current density=7.14 mA/cm^2 *T*=25 ℃	97.76% (in 1st cycle) above 97% (in 10th cycle)
Pt-plating titanium (50 mm×35 mm)	**ACF coating Pt-plating titanium cathode** (50 mm×35 mm)	[100]	[Carbamazepine]$_0$=0.042 mM [PDS]$_0$=100 mM *t*=30 min pH$_{solution}$=3 (adjusted) Working voltage=6 V *T*=25 ℃	98.78% (in 1st cycle) 97.35% (in 100th cycle)
$BiVO_4$ photoanode (1 × 1 cm^2)	**$MnFe_2O_4$ coating Carbon paper (CFP) cathode**	[104]	[Bisphenol A]$_0$=10 mg/L [PMS]$_0$=1 mM *t*=90 min pH$_{solution}$ not reported Working voltage=1 V *T*=20 ℃ Xenon lamp (300 W)	100% (in 1st cycle) About 85% (in 5th cycle)
$BiVO_4$ photoanode (16 cm^2)	**PDA coating carbon felt (CF) cathode** (16 cm^2)	[105]	[Ofloxacin]$_0$=0.04 mM [PMS]$_0$=2 mM *t*=120 min pH$_{solution}$=5 (buffered) Working voltage=1.5 V *T* not reported	100% (in 1st cycle) above 90% (in 5th cycle)

			Xenon lamp (300 W)	
Platinum-plated titanium (5.0×3.5 cm)	**ACF coating Pt-plating titanium cathode** (0.2 g, 5.0 cm×3.5 cm×3 mm)	[99]	$[Phenol]_0$=1600 mg/L $[PDS]_0$=100 mM $[Na_2SO_4]$=0.2 M *t*=6 h $pH_{solution}$ not reported (unadjusted) Current intensity=1 A *T*=25 °C	66% (in 1st cycle) 34.12% (in 4th cycle)
Not reported	**Carbonized wood cathode** (4.0 cm×2.0 cm×0.8 cm)	[102]	$[Phenol]_0$=20 mg/L $[PMS]_0$=6.51 mM $[Na_2SO_4]$=50 mM *t*=10 min $pH_{solution}$=2.87 (unadjusted) Current density=2.75 mA/cm^2 *T*=25 °C Flow rate=0.5 mL/min	97.9% (in 1st cycle) 98.4% (in 2nd cycle) 98.0% (in 3rd cycle) 97.6% (in 4th cycle) 97.9% (in 5th cycle)